CFD Predictions for Flow-Regime Transitions in Bubble Columns

Sarah M. Monahan, Vivek S. Vitankar, and Rodney O. Fox
Dept. of Chemical Engineering, Iowa State University, Ames, IA 50011

DOI 10.1002/aic.10425

This work evaluates the ability of multiphase computational fluid dynamics (CFD) models to predict known flow regimes in air–water bubble columns. An initial grid-resolution study shows that grid spacing of 0.25 cm or smaller must be used for adequate resolution. The ability of the two-fluid model to predict homogeneous- and transitional-flow behavior is analyzed next, and the flow predictions are found to be highly dependent on the model formulation (that is, bubble-induced turbulence, drag, virtual mass, lift, rotation, and strain). At low gas velocities, homogeneous flow is observed for only a particular set of force models. At higher gas velocities, the same set of models yields reasonable predictions of transitional flow for small columns. Bubble size and liquid coflow also affect flow structures and flow stability at high gas flow rates. Scale-up to larger column diameters is studied for both the homogeneous- and transitional-flow regimes. In the homogeneous regime, the flow behavior is found to be independent of column diameter. However, because of neglect of coalescence, transition to churn-turbulent flow is not observed at high gas velocities for large column diameters. © 2005 American Institute of Chemical Engineers *AIChE J,* 51: 1897–1923, 2005

Keywords: computational fluid dynamics, gas–liquid flow, bubbly flow, buoyancy driven flow, two-fluid model, flow transitions

Introduction

Bubble-column reactors have widespread applications in the chemical industry because of their simple construction and ease of operation. Because of the large interfacial area available, bubble columns offer excellent heat- and mass-transfer characteristics and thus are the reactors of choice for slow chemical reactions and exothermic or endothermic processes.[1]

The movement of bubble plumes and the chaotic three-dimensional (3-D) vortical structures dominate bubble-column hydrodynamics.[2] For this reason, computational fluid dynamics (CFD) has been promoted as a useful tool for understanding bubble-column flow behavior.[3] The bubble-rise velocity, bubble–bubble interactions, bubble–fluid interactions, bubble shape and size distribution, gas holdup, and interstitial liquid velocities determine the hydrodynamic behavior of the column, a thorough understanding of which is important for reliable design of bubble columns. Several authors[3-8] have discussed recent developments in the fields of modeling and CFD simulation. A literature study reveals the use of simple one-dimensional models,[9-12] two-dimensional (2-D) gas–liquid mixture models,[13-16] 2-D and 3-D turbulent CFD approaches for flow-field computations combined with a compartmental model for handling chemistry computations,[17] 2-D and 3-D two-fluid turbulent models with variations in the formulation of the Euler–Euler or the Eulerian–Lagrangian approach,[18-34] and large-eddy simulation (LES) attempts.[35,36]

In our previous work with the two-fluid model,[37] it was observed that grid-independent CFD simulations of air–water bubble columns are sensitive to the physical models and chosen parameters used in the simulations. A similar conclusion was reported by Sundaresan[38] for gas–solid flows. However, unlike for gas–solid flows, there is no general consensus in the literature as to the correct two-fluid model formulation for gas–

Correspondence concerning this article should be addressed to S. M. Monahan at monahan@iastate.edu.

liquid flows, or on the ability of CFD models to predict experimentally observed flow regimes.[7] For example, Delnoij et al.[21-23] considered detailed bubble–bubble interactions in the laminar-flow model along with drag, lift, virtual-mass, and hydrodynamic-interaction forces to simulate two-phase flow in a flat bubble column using a Eulerian–Lagrangian approach. Sokolichin and Eigenberger[24] obtained similar results with a highly simplified version of the gas-phase momentum balance, neglecting the virtual-mass, lift, and hydrodynamic forces, and with no account of bubble–bubble interactions, but with a finer grid size. Delnoij et al.[22] obtained an expected spread in the bubble plume when considering the lift force in their simulations. They observed the effect of the virtual-mass force only in the near sparger region. Further, they observed that the inclusion of the virtual-mass force contributed to the stability of the solution. Deen et al.[35] did not observe any effect of the virtual-mass force. Krishna and van Baten[39] considered only the drag force in their elevated pressure turbulent-flow simulations; they claim that there is much uncertainty when considering lift forces for both small and large bubbles, and that the virtual-mass force is not applicable because the large bubbles present in this flow regime experience a high degree of recirculation and do not have closed wakes. However, Jakobsen[40] considered the importance of both steady drag and transversal lift forces for phase distribution in bubble columns, ultimately concluding that numerical models required further improvements in accuracy and stability. Oey et al.[33] found that the drag force was acceptable for representing global bubble-column dynamics, whereas the virtual-mass force served as a means of tuning the simulation results. They also noted that further research regarding the importance of the lift force was necessary. The recent review paper from Sokolichin et al.,[7] however, suggests that pressure and drag are the only relevant forces for bubble column simulations.

Other authors have used multiphase turbulence models to treat the same class of gas–liquid flows. For example, Becker et al.[41] and Mudde and Simonin[25] obtained a damped circulatory flow with the 2-D k–ε model, whereas 3-D k–ε simulations[25] resulted in a transient solution. Other researchers[14,21-24,41] obtained meandering-plume behavior with the laminar model. Becker et al.[41] obtained a stationary result with a coarse grid (6×2.78 cm^2), whereas with a finer grid (3×1.39 cm^2), a transient solution was obtained. Sokolichin and Eigenberger[24] also investigated the effect of grid size for the laminar model using five different grids (2×2; 1×1; 0.5×0.5; 0.25×0.25; 0.125×0.125 cm^2). The number of circulation cells resolved by the simulations was found to increase with increasing spatial resolution.

Bubble–bubble interactions and coalescence also play a significant role in the flow behavior observed. The understanding of the basic phenomena of bubble–bubble interactions and how to include them in CFD models are still in their early stages. Duinveld[42] carried out detailed experiments to study the bouncing and coalescence phenomena of bubbles. He has shown that these phenomena can be determined by the Weber number, based on either the rise velocity of the bubbles or the approach velocity of the bubbles. The liquid between two bubbles moving toward each other opposes the resulting relative motion. This relative motion causes an increase in the pressure in the film between the bubbles, which in turn drives the liquid outward from the film. The bubbles bounce if the pressure in the liquid film reaches a magnitude for which the relative motion of the bubbles ceases. Otherwise, bubble coalescence takes place.[22] These interactions result in additional turbulence in the liquid phase, which is not directly accounted for in most two-fluid models.

Sato et al.[43] developed a bubble-induced turbulence (BIT) model for bubbly flows. Given that the characteristic length scale is the bubble diameter, Sato's BIT model can be interpreted as a description of momentum transport induced by the bubble wakes. Even at low gas flow rates where the liquid phase is laminar away from the bubble wakes, the Reynolds number (Re) based on the bubble rise velocity is typically large (Re $= 26$–1093 in this work). Thus, the BIT model would still be applicable for gas–liquid flows. On the other hand, at high gas flow rates the momentum transfer from the gas phase can be high enough to induce large-scale turbulence in the liquid phase. In fully turbulent two-phase flows, this contribution to the liquid-phase turbulence can be modeled through an extra source term in the k–ε turbulence model. Several researchers[44-47] have developed such source terms, and Lain et al.[6] developed a consistent Lagrangian formulation of the source terms attributed to bubbles in the k and ε equations. We should note, however, that the use of two-phase turbulence models is difficult to justify at low gas flow rates where velocity fluctuations are generated by bubble wakes. At best, such models may apply for churn-turbulent flow, but still rest on weak physical grounds in comparison to single-phase turbulence models.

A general overview of the approaches, physical models, and grid sizes used in the literature for air–water bubble columns is summarized in Table 1.[4,6,13-16,19,21-26,28-31,34-37,41,48-53] It can be observed that important aspects such as (1) bubble–bubble interactions; (2) two-phase turbulence modeling; (3) gas–liquid interfacial mass, momentum, and energy-transfer mechanisms; (4) coupling between the phases; and (5) the required grid resolution still need to be resolved. Moreover, as a general rule, most literature studies have been limited to the prediction of one particular flow regime (such as churn-turbulent flow). (The works of Olmos et al.[34,54,55] are notable exceptions.) Thus, the ability of CFD models to predict flow-regime transitions arising from changes in the gas flow rate and/or column diameter has yet to be convincingly demonstrated. For example, at low gas velocities it is known experimentally that a homogeneous bubbly-flow regime prevails wherein the gas phase is uniformly distributed and rises vertically with no large-scale flow structures.[56,57] In contrast, grid-independent CFD simulations for this case with "standard" two-fluid models exhibit highly turbulent, inhomogeneous two-phase flow.[37] This mismatch between simulation and experiments calls into question the basic validity of two-fluid CFD models for gas–liquid flows, as presently formulated, and provides motivation for a careful investigation of their true capabilities.

The present work describes our attempts to predict flow behavior in air–water bubble columns with uniform sparging and constant-diameter, noncoalescing bubbles. This configuration is motivated by the recent experiments of Garnier et al.[56,57] and Harteveld et al.[58] These carefully designed experiments provide valuable insights into the effects of operating conditions on the homogeneous- and transitional-flow regimes. We begin with a brief analysis of the effect of wall boundary conditions, followed by a thorough grid-resolution study,

Table 1. Summary of Previous Work on Numerical Simulation of Air–Water Bubble Columns

		Solution Procedure				
Reference	Approach	Model	Drag	Lift	VM	Grid Cell Size (cm) (H × W × D)
4	Euler–Euler	2-D axisymmetric, modified k–ε model	(aa)	(f) $C_L = 0.5$	(g) $C_{vm} = 0.2$	15 × 29 cells in computational grid; refer to paper for test cases
6	Euler–Lagrange	2-D axisymmetric, Std. k–ε model	(l)	(f) $C_L = 0.5$	(g) $C_{vm} = 0.5$	0.433 × 0.28; 0.295 × 0.2
13	Euler–Euler	Laminar 2-D	(p)	NC	NC	1 × 0.6
14	Euler–Euler, Euler–Lagrange	Laminar 2-D	(a)	NC	NC	1 × 1
15	Euler–Euler	2-D axisymmetric, Std. k–ε model	(v)	NC	NC	0.66 × 0.5
16	Mixture Eqs., RANS	2-D axisymmetric, Std. k–ε model	NC	NC	NC	3.2 × 1.4; 1.6 × 0.7
19	Euler–Euler, Euler–Lagrange	Population balance 2-D	(a)	NC	NC	Nonuniform grid with 60 × 200 rectangular cells, with higher refinement near column walls
21, 22	Euler–Lagrange	Laminar 2-D	(b)	(c)	(d)	1.5 × 1
23	Euler–Lagrange	Laminar Pseudo-2-D	(b)	(c) $C_L = 0.53$	(d)	0.875 × 0.875
24	Euler–Euler	2-D, 3-D, Laminar, and Std. k–ε model	(a)	NC	NC	2-D: 2 × 2; 1 × 1; 0.5 × 0.5; 0.25 × 0.25; 0.125 × 0.125 3-D: 2 × 2 × 2; 1 × 1 × 1; 0.667 × 0.667 × 0.667
25	Euler–Euler	2-D, 3-D, Std. k–ε model, low Reynolds k–ε model	(t)	NC	(u) $C_{vm} = 0.5$	3 × 2; 3 × 1.39; 3 × 2 × 1; 3 × 1.39 × 0.5
26	Euler–Euler	2-D, Sato's model	(q)	NC	(h)	0.8 × 0.5 in general, more refined near air injectors
28	Euler–Euler	3-D, Std. k–ε model with BIT by additional production terms in k–ε equations	(e) $C_D = 0.44$	NC	NC	Quadrilateral cells in number ranging from 6150 (coarsest) to 62,400 (finest); standard is 12,300 cells
29	Euler–Euler	3-D, Std. k–ε model	(m)	(o)	(n)	Quadrilateral cells in number ranging from 2975 (coarsest) to 106,628 (finest); midrange is 16,544 cells
30	Euler–Euler	3-D, k–ε model including shear and bubble-induced terms	(z)	NC	NC	Block structured grid with volume elements having edges 1–2 cm long
31	Euler–Euler	3-D, Std. k–ε model	(e) $C_D = 0.44$	NC	NC	Coarse grid with average cell length of 5.9 cm, resulting in 13,600 total cells
34	Multiple gas phase Euler–Euler	Population balance, 2-D axisymmetric, Std. k–ε model or Sato's model	(r)	NC	NC	0.5 × 0.5
35	Euler–Euler	3-D, Std. k–ε model and LES	(e) $C_D = 1.0$	(f) $C_L = 0.5$	(g) $C_{vm} = 0.5$	1 × 1 × 1
36	Euler–Euler	3-D, Sato's model, VLES	(s)	(f) $C_L = 0.5$	(g) $C_{vm} = 0.5$	1.5 × 2.5 × 2.5; 1.5 × 1.67 × 1.67; 1 × 1 × 1
37	Euler–Euler	2-D, Laminar	(j)	(i)	(k) $C_{vm} = 0.5$	1 × 1; 0.5 × 0.5; 0.25 × 0.25
41	Euler–Euler	2-D, Laminar viscosity increased by factor of 100	(p)	NC	NC	6 × 2.78 3 × 1.39
48	Euler–Lagrange	Laminar 3-D	(b)	(c) $C_L = 0.53$	(d)	0.875 × 0.875 × 0.875

Table 1. Continued

Reference	Approach	Solution Procedure				Grid Cell Size (cm) (H × W × D)
		Model	Drag	Lift	VM	
49	Three-phase Euler–Euler	3-D cylindrical Std. k–ε model	(w)	NC	NC	4800 total cells. Radial: 10 cells in central core region, 20 cells near wall region Axial: 1 cm cells in first 20 cm at column bottom, 2 cm cells for remainder of column
50	Euler–Euler	Std. k–ε model 2-D, 3-D	(e) $C_D = 0.66$	NC	NC	Standard grid has 40,000 cells; coarsest is 45 × 22 × 5 cells and finest is 90 × 44 × 15 cells
51	Euler–Euler	3-D conical domain, multiphase k–ε model	(x)	NC	(y) $C_{vm} = 0.5$	Cells have 8 vertices and 6 faces; mesh uses 67 blocks with 4620 real cells, and 20,280 ghost cells for interblock communication

(a) Constant slip velocity

(b)

$$\boldsymbol{F}_D = -\frac{1}{2}C_D\rho_c r_b^2\pi|\boldsymbol{u}_d - \boldsymbol{u}_c|(\boldsymbol{u}_d - \boldsymbol{u}_c),\ C_D = \begin{cases}\dfrac{24}{\mathrm{Re}}(1 + 0.15\,\mathrm{Re}^{0.687}), & \mathrm{Re} < 1000\\ 0.44, & \mathrm{Re} \geq 1000\end{cases}$$

(c) $\boldsymbol{F}_L = -C_L\rho_c V_b(\boldsymbol{u}_d - \boldsymbol{u}_c) \times (\boldsymbol{\nabla} \times \boldsymbol{u}_c)$

(d)

$$\boldsymbol{F}_{vm} = -\left[\left(\frac{\partial \boldsymbol{I}}{\partial t} + \boldsymbol{u}_d \cdot \boldsymbol{\nabla}\boldsymbol{I}\right) + \boldsymbol{I}\cdot\boldsymbol{\nabla}\boldsymbol{u}_c\right],\ \boldsymbol{I} = C'_{vm}\rho_c V_b(\boldsymbol{u}_d - \boldsymbol{u}_c),\ C'_{vm} = 0.5[1 + 2.78(1 - \alpha_c)]$$

(e)

$$\boldsymbol{F}_D = -\frac{3}{4}\frac{C_D}{d_b}\alpha_d\rho_c|\boldsymbol{u}_d - \boldsymbol{u}_c|(\boldsymbol{u}_d - \boldsymbol{u}_c)$$

(f) $\boldsymbol{F}_L = C_L\alpha_d\rho_c(\boldsymbol{u}_d - \boldsymbol{u}_c) \times \boldsymbol{\nabla} \times \boldsymbol{u}_c$

(g)

$$\boldsymbol{F}_{vm} = -\alpha_d\rho_c C_{vm}\left[\left(\frac{\partial \boldsymbol{u}_d}{\partial t} + \boldsymbol{u}_d\cdot\boldsymbol{\nabla}\boldsymbol{u}_d\right) - \left(\frac{\partial \boldsymbol{u}_c}{\partial t} + \boldsymbol{u}_c\cdot\boldsymbol{\nabla}\boldsymbol{u}_c\right)\right]$$

(h)

$$\boldsymbol{F}_{vm} = -\frac{1}{2}\alpha_c\alpha_d C_{vm}\rho_c\left[\left(\frac{\partial \boldsymbol{u}_d}{\partial t} + \boldsymbol{u}_d\cdot\boldsymbol{\nabla}\boldsymbol{u}_d\right) - \left(\frac{\partial \boldsymbol{u}_c}{\partial t} + \boldsymbol{u}_c\cdot\boldsymbol{\nabla}\boldsymbol{u}_c\right)\right],\ C_{vm} = 1 + 3.32\alpha_d + O(\alpha_d^2)$$

(i) $\boldsymbol{F}_L = \alpha_d\alpha_c\rho_v C_L(\boldsymbol{u}_d - \boldsymbol{u}_c) \times \boldsymbol{\nabla} \times \boldsymbol{u}_c$

(j)

$$\boldsymbol{F}_D = -\alpha_d\alpha_c\rho_c C_D(\mathrm{Re})\frac{3}{4d_b}|\boldsymbol{u}_c - \boldsymbol{u}_d|(\boldsymbol{u}_d - \boldsymbol{u}_c),\ C_D(\mathrm{Re}) = 0.5 + \frac{24}{\mathrm{Re}} + \frac{6}{1 + \sqrt{\mathrm{Re}}}$$

(k)

$$\boldsymbol{F}_{vm} = -\alpha_d\alpha_c\rho_v C_{vm}\left[\left(\frac{\partial \boldsymbol{u}_d}{\partial t} + \boldsymbol{u}_d\cdot\boldsymbol{\nabla}\boldsymbol{u}_d\right) - \left(\frac{\partial \boldsymbol{u}_c}{\partial t} + \boldsymbol{u}_c\cdot\boldsymbol{\nabla}\boldsymbol{u}_c\right)\right]$$

(l)

$$\boldsymbol{F}_D = \frac{3}{4}\alpha_d\frac{\rho_c}{d_b}C_D(\boldsymbol{u}_c - \boldsymbol{u}_d)|\boldsymbol{u}_c - \boldsymbol{u}_d|$$

$$C_D = \begin{cases}16\,\mathrm{Re}^{-1} & \mathrm{Re} < 1.5\\ 14.9\,\mathrm{Re}^{-0.78} & 1.5 < \mathrm{Re} < 80\\ 48\,\mathrm{Re}^{-1}(1 - 2.21\,\mathrm{Re}^{-0.5}) + (1.86 \times 10^{-15})\mathrm{Re}^{4.756} & 80 < \mathrm{Re} < 1500\\ 2.61 & 1500 < \mathrm{Re}\end{cases}$$

(m)

$$\boldsymbol{F}_D = -\alpha_d\alpha_c\rho_c C_D(\mathrm{Re})\frac{3}{4d_b}|\boldsymbol{u}_c - \boldsymbol{u}_d|(\boldsymbol{u}_d - \boldsymbol{u}_c)$$

$$C_D(\mathrm{Re}) = \max\left\{\frac{24}{\mathrm{Re}}(1 + 0.15\,\mathrm{Re}^{0.687}),\ \frac{8}{3}\left(\frac{\mathrm{Eo}}{\mathrm{Eo} + 4}\right)\right\},\ \mathrm{Eo} = \frac{\boldsymbol{g}|\rho_c - \rho_d|d_b^2}{\tau}$$

(n)

$$\boldsymbol{F}_{vm} = 0.5\rho_c\alpha_d\alpha_c\left(\frac{\partial \boldsymbol{u}_c}{\partial t} - \frac{\partial \boldsymbol{u}_d}{\partial t}\right)$$

(o) $\boldsymbol{F}_L = -0.5\rho_c\alpha_d\alpha_c(\boldsymbol{u}_c - \boldsymbol{u}_d) \times (\boldsymbol{\nabla} \times \boldsymbol{u}_c)$

(p) $\boldsymbol{F}_D = -5 \times 10^4\alpha_d(\boldsymbol{u}_d - \boldsymbol{u}_c)$

(q)

$$\boldsymbol{F}_D = \frac{1}{2}\rho_c r_b^2 C_D\pi|\boldsymbol{u}_c - \boldsymbol{u}_d|(\boldsymbol{u}_c - \boldsymbol{u}_d)$$

$$C_D = \max\left[\frac{24}{\mathrm{Re}}(1 + 0.15\,\mathrm{Re}^{0.687}),\ \frac{8}{3}\frac{\mathrm{Eo}}{\mathrm{Eo} + 4}\right],\ \mathrm{Eo} = \frac{\boldsymbol{g}\rho_c d_b^2}{\tau}$$

Table 1. Continued

(r)

$$\boldsymbol{F}_D = -\frac{3}{4} C_D \alpha_d \rho_c \frac{1}{d_b} |\boldsymbol{u}_c - \boldsymbol{u}_d| (\boldsymbol{u}_d - \boldsymbol{u}_c),\ d_b \text{ used is Sauter mean diameter}$$

$$C_D = C'_D (1 - \bar{\alpha}_d)^p,\ p \text{ is experimentally determined}$$

$$C'_D = \frac{2}{3} \sqrt{\mathrm{Eo}} \approx 1.2, \text{ uniform aeration, low superficial gas velocities, drag-distorted model}$$

$$C'_D = \frac{8}{3}, \text{ spherical cap regime}$$

(s)

$$F_D = -\frac{3}{4} \frac{C_D}{d_b} \alpha_d \rho_c |\boldsymbol{u}_c - \boldsymbol{u}_d| (\boldsymbol{u}_d - \boldsymbol{u}_c)$$

$$C_D = \frac{2}{3} \sqrt{\mathrm{Eo}}, Eo = \frac{g(\rho_c - \rho_d) d_b^2}{\tau}, \text{ drag}-\text{distoreted model}$$

contaminated water model [52]

$$C_D = \frac{4}{3} \frac{(\rho_c \rho_d) \mathbf{g} d_b}{\rho_c U_T^2}$$

$$U_T = \frac{\sin^{-1} \sqrt{1 - E^2} - E \sqrt{1 - E^2}}{1 - E^2} \sqrt{\frac{8\tau}{\rho_c d_b} E^{4/3} + \frac{(\rho_c - \rho_d) \mathbf{g} d_b}{2\rho_c} \frac{E^{2/3}}{1 - E^2}},\ E = \frac{1}{1 + 0.163\ \mathrm{Eo}^{0.757}}$$

(t)

$$\boldsymbol{F}_D = \frac{3}{4} \frac{C_D}{d_b} \alpha_d \rho_c \boldsymbol{u}_r \sqrt{\boldsymbol{u}_r \cdot \boldsymbol{u}_r + \langle \boldsymbol{u}''_r \cdot \boldsymbol{u}''_r \rangle_d}$$

$$C_D = \frac{24}{\mathrm{Re}} (1 + 0.15\ \mathrm{Re}^{0.687}) \alpha_c^{-1.7}, \text{ if } \mathrm{Re} < 1000$$

$$\mathrm{Re} = \frac{\alpha_c \rho_c |\boldsymbol{u}_r| d_b}{\mu_c},\ \boldsymbol{u}_r = (\boldsymbol{u}_d - \boldsymbol{u}_c) - \boldsymbol{u}_{drift},\ \boldsymbol{u}_{drift} = \langle \boldsymbol{u}''_c \rangle_d$$

(u)

$$\boldsymbol{F}_{vm} = \alpha_d \rho_c C_{vm} \left[\frac{\partial \boldsymbol{u}_r}{\partial t} + \boldsymbol{u}_d \cdot \boldsymbol{\nabla} \boldsymbol{u}_r \right] + \boldsymbol{\nabla} \cdot \alpha_d \rho_c C_{vm} \langle \boldsymbol{u}''_d \boldsymbol{u}''_r \rangle_2$$

$$\boldsymbol{u}_r = (\boldsymbol{u}_d - \boldsymbol{u}_c) - \boldsymbol{u}_{drift},\ \boldsymbol{u}_{drift} = \langle \boldsymbol{u}''_c \rangle_d$$

(v) Single sphere drag correlation[53]

(w)

$$\boldsymbol{F}_D = -\frac{3}{4} \rho_c \frac{\alpha_d}{d_b} C_D (\boldsymbol{u}_d - \boldsymbol{u}_c) |\boldsymbol{u}_d - \boldsymbol{u}_c|$$

$$C_D = \frac{4}{3} \frac{\rho_c - \rho_d}{\rho_c} \boldsymbol{g} d_b \frac{1}{U_T^2}, \text{ calculation for } U_T \text{ dependent on bubble size}^{49}$$

(x)

$$\boldsymbol{F}_D = \alpha_c \alpha_d \frac{3}{4} \rho_{cd} C_D \frac{|\boldsymbol{u}_c - \boldsymbol{u}_d|}{d_b} (\boldsymbol{u}_c - \boldsymbol{u}_d),\ C_D = 1.0 + \frac{24}{\mathrm{Re}} + \frac{6}{(1 + \sqrt{\mathrm{Re}})}$$

$$\rho_{cd} = \frac{1}{2} \left\{ (\rho_c + \rho_d) - (\rho_c - \rho_d) \tanh \left[\frac{2(\alpha_d - 0.5)}{\alpha_d (1 - \alpha_d)} \right] \right\}$$

(y)

$$\boldsymbol{F}_{vm} = -\alpha_c \alpha_d \rho_{cd} C_{vm} \left[\left(\frac{\partial \boldsymbol{u}_d}{\partial t} + \boldsymbol{u}_d \cdot \boldsymbol{\nabla} \boldsymbol{u}_d \right) - \left(\frac{\partial \boldsymbol{u}_c}{\partial t} + \boldsymbol{u}_c \cdot \boldsymbol{\nabla} \boldsymbol{u}_c \right) \right]$$

$$\rho_{cd} = \frac{1}{2} \left\{ (\rho_c + \rho_d) - (\rho_c - \rho_d) \tanh \left[\frac{2(\alpha_d - 0.5)}{\alpha_d (1 - \alpha_d)} \right] \right\}$$

(z)

$$\boldsymbol{F}_D = -\frac{3}{4} \rho_c \frac{\alpha_d}{d_b} C_D |\boldsymbol{u}_d - \boldsymbol{u}_c| (\boldsymbol{u}_d - \boldsymbol{u}_c), C_D = \max \left\{ \frac{24}{\mathrm{Re}} (1 + 0.1 \mathrm{Re}^{0.75}) \min \left[\max \left(0.44, \frac{2}{3} \mathrm{Eo}^{1/2} \right), \frac{8}{3} \right] \right\}$$

$$\mathrm{Re} = \frac{\rho_c |\boldsymbol{u}_c| d_b}{\mu_c},\ \mathrm{Eo} = \frac{\boldsymbol{g}(\rho_c - \rho_d) d_b^2}{\tau},\ d_b \text{ used is Sauter mean diameter}$$

(aa)

$$\boldsymbol{F}_D = \frac{3}{4} \frac{\alpha_d}{d_S} \left(\frac{d_S}{d_D} \right) \rho_c C_D |\boldsymbol{u}_c - \boldsymbol{u}_d| (\boldsymbol{u}_c - \boldsymbol{u}_d),\ C_D = \frac{0.622}{(1.0/\mathrm{Eo}) + 0.235},\ \mathrm{Eo} = \frac{\boldsymbol{g} |\rho_c - \rho_d| d_S^2}{\tau}$$

* d_S denotes Sauter mean diameter, d_D denotes drag diameter

* Turbulent transversal drag contribution also considered.[4] NC, not considered.

which is performed initially to determine the required resolution for grid-independent results. The major conclusion of the grid-resolution study is that nearly all of the previous results for two-fluid CFD models reported in the literature for air–water bubble columns are contaminated by numerical diffusion. It is also clear from this study that the laminar two-fluid model

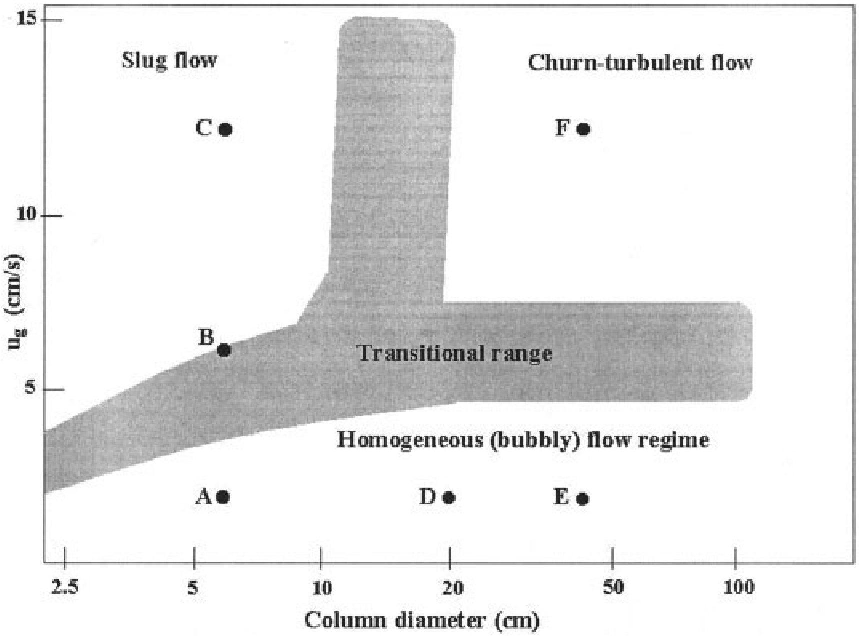

Figure 1. Flow-regime map (adapted from Shah and Deckwer[2]) and markers indicating cases studied in the present work.

(A) 6-cm column with inlet air velocity of 2 cm/s. (B) 6-cm column with inlet air velocity of 6.2 cm/s. (C) 6-cm column with inlet air velocity of 12 cm/s. (D) 20-cm column with inlet air velocity of 2 cm/s. (E) 40-cm column with inlet air velocity of 2 cm/s. (F) 40-cm column with inlet air velocity of 12 cm/s. Note that this map does not account for the effect of bubble size.

predicts (incorrectly) heterogeneous flow for low gas velocities (such as 2 cm/s).

In an attempt to homogenize the bubble volume-fraction distribution, the bubble-pressure (BP) model proposed by Biesheuvel and Gorissen[59] is implemented. However, the BP model alone proves to be insufficient to generate homogeneous flow. Because it is well known that flow instabilities are dampened by an increase in the effective viscosity,[60] the BIT model is then included in the formulation. Although the BIT model stabilizes the flow for particular values of the bubble diameter, it also proves to be insufficient to generate homogeneous flow where expected experimentally. Thus, the effects of other interphase-force models are studied next to determine which force models (if any) are needed for the two-fluid model to successfully predict homogeneous flow. A particular set (which includes drag, virtual mass, lift, rotation, and strain) is identified, and the same set is then shown to predict a transition to "slugging" flow in the correct range as the gas flow rate is increased. For high-gas-flow-rate simulations, analyses of both the effect of bubble diameter on flow structures and the effect of liquid coflow on flow stability are presented. Finally, the combined influence of the BIT model and the force models is discussed for scale-up to different column diameters (6, 20, and 40 cm). Although the CFD model at high gas flow rates and with large-diameter columns does not predict churn-turbulent flow, strong segregation of the bubble phase is observed. We speculate that such high local values of the bubble volume fraction should lead to bubble coalescence, followed by transition to the churn-turbulent regime. Thus, because coalescence is not accounted for in our study, the transition to churn-turbulent flow is not observed.

The remainder of this work is arranged as follows. First, we briefly review the experimental data for flow regimes in bubble columns and discuss two recent experiments on homogeneous bubbly flow that motivated our work. Then, an overview of the CFD modeling approach is presented, along with a discussion of the important terms in the two-fluid model for gas–liquid flow. The simulation results are presented next, and the ability of the two-fluid model to predict the experimentally observed flow regimes is analyzed. Conclusions are drawn in the final section, where plans for future work are also discussed briefly.

Bubble-Column Flow Regimes

Depending on the inlet flow conditions, two primary flow regimes can be identified for bubble-column flows: homogeneous and heterogeneous. A flow-regime map for air–water bubble columns, based on column diameter and inlet air velocity (u_g), is given in Figure 1. (Both Figures 1 and 2 are adapted from Shah and Deckwer.[2]) Note that the flow-regime map does not account for bubble diameter; however, Shah and Deckwer[2] suggest that the representative stable bubble diameter is near 4 mm. It should be noted that the map is overall qualitative and is used primarily to define the difference between homogeneous and heterogeneous flows. Figure 2 illustrates qualitative representations of homogeneous flow, slug flow, and churn-turbulent flow, each of which will be discussed in this section. Note that for slug and churn-turbulent flows bubble coalescence is significant and most likely has a predominate effect on these flows. Markers are superimposed onto Figure 1 to designate the expected flow regimes for the cases studied in the present work. The homogeneous, or bubbly-flow, regime is characterized by low gas velocities (<5 cm/s) and bubbles that tend to be small, uniform, and approximately

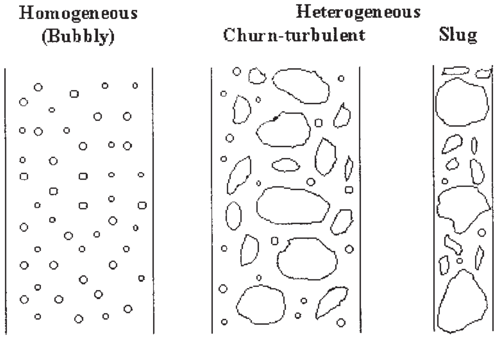

Figure 2. Representations of flow regimes observed in bubble columns.

spherical in shape. In this regime, the bubbles have nearly equal rise velocities, travel rectilinearly upward, and exhibit little interaction with neighboring bubbles.[2]

Recent experiments have demonstrated that the use of low air inlet flow rates and uniform feed in small-diameter bubble columns results in homogeneous flow behavior. Garnier et al.[56,57] used a cylindrical air–water bubble column with a diameter of 8 cm. The column height was fixed at 31 cm for this particular experiment. Air was injected through a system of needles at the bottom of the column, and the injection device was designed to maintain a nearly uniform distribution of air. Water was introduced perpendicular to the needles, and then traveled upward through the column. Experiments were conducted for four values of the superficial liquid velocity: 1.6, 3.3, 4.4, and 6.2 cm/s. Velocity and holdup profiles were overall uniform for these experiments. By suppressing bubble coalescence, Garnier et al.[56,57] were able to observe the transition from laminar to turbulent homogeneous flow by increasing the gas velocity. Unlike the slug-flow regime shown in Figure 2, the turbulent homogeneous-flow regime exhibits large velocity fluctuations attributed to the rapid, coherent motion of "bubble swarms." In an independent experimental study, Harteveld et al.[58] used a 15-cm cylindrical bubble column, initially filled with tap water to a height of 130 cm. Air-injection needles were organized in groups to allow both uniform and nonuniform feed. For uniform aeration, air was introduced at 2.3 cm/s. As expected from Figure 2, the resulting radial gas holdup profiles were uniform except at the column walls. Most inhomogeneous flow behavior caused by the bubble injection system disappeared at a height of 15 cm (that is, the homogeneous flow was stable to initial fluctuations). However, these authors show that the bubble-flow behavior is strongly influenced by nonuniform feed (that is, by changing the inlet boundary conditions for the gas phase). For example, when bubbles are injected uniformly except for a region near the wall where no bubbles are introduced, a transition to swirling bubbly flow is observed. Although beyond the scope of this work, this sensitivity of homogeneous flow to the inlet boundary conditions offers a valuable database for testing the predictive abilities of two-fluid CFD models.

As the gas flow rate is increased, transition to the heterogeneous-flow regime will eventually occur. Bubbles of different sizes and shapes and intense liquid circulation are typical for this regime.[61] The relatively high gas holdup and vigorous velocity fluctuations lead to bubble coalescence, which further enhances flow instabilities. At high gas velocities, slug flow occurs in small-diameter columns, whereas churn-turbulent flow occurs in large-diameter columns.[2] Churn-turbulent flow is observed in most industrial applications, and is characterized by large bubbles traveling primarily in the center of the column. As gas velocity increases, gas is more likely to be transported by large bubbles and bubble clusters.[2] Slug flow occurs in small-diameter columns when large bubbles are stabilized by the column walls to form slugs, as shown in Figure 2. Such behavior usually is not observed for columns of industrial size. Although bubble clusters approximately 10 cm in diameter can be observed in bubble columns, slugs typically do not form in columns larger than about 15 cm in diameter.[2]

Olmos et al.[55] observed two transitional regimes in between the homogeneous- and heterogeneous-flow regimes. Their experiments for a 20-cm column demonstrated that homogeneous flow was dominant for superficial gas velocities < 3.2 cm/s. For gas velocities between 3.2 and 4.4 cm/s (the first transitional regime), holdup increased at a slower rate, and coalescence occurred near the sparger, resulting in a plume. However, this plume broke apart after reaching a definitive liquid height, after which the flow regime again appeared homogeneous. Holdup values remained nearly constant when the superficial gas velocity was between 4.4 and 5.5 cm/s (the second transitional regime), and the height of the plume increased with increasing superficial velocity. The heterogeneous regime was observed for superficial gas velocities > 5.5 cm/s, and was characterized by varied bubble sizes, with the largest bubbles located in the center of the column, as described by Shah and Deckwer.[2]

As noted in the introduction, much of the recent CFD work on bubble columns has focused on the predictions of time-averaged quantities such as gas holdup in the churn-turbulent regime.[7,26,29,32,49] As shown in this work, such studies are of limited utility for determining the predictive ability of two-fluid CFD models for gas–liquid flows, and for discriminating between different model formulations. For example, we show that the drag-force model primarily determines the time-averaged gas holdup, and thus the same value is obtained for laminar, homogeneous flow and for turbulent, heterogeneous flow. Thus, because the drag-force model is a correlation that must be input into the CFD model, comparison of time-averaged gas holdup only confirms the adequacy of the correlation while resting mute on the predictive abilities of the two-fluid model. For this reason, we focus our attention in this work on the ability of CFD models to predict instantaneous flow patterns and transitions between known flow regimes with uniform inlet boundary conditions as observed in the experiments of Garnier et al.[56,57] and Harteveld et al.[58] In particular, we seek to answer the question of whether the two-fluid model can predict the homogeneous- and transitional-flow regimes shown in Figure 1. In our opinion, only after answering this question in the affirmative can CFD model validation for nonuniform inlet boundary conditions and for the churn-turbulent regime be undertaken with any confidence in the generality of the conclusions.

Computational Approach

The code used for the numerical studies is CFDLib v.99.2,[62,63] a multiphase simulation library developed at Los

Alamos National Laboratory (Los Alamos, NM). The same code has been used by Pan et al.,[26,27] Padial et al.,[51] and Chen and Fan[8] for simulating gas–liquid bubble columns. CFDLib uses a finite-volume technique to integrate the time-dependent equations of motion that govern multiphase flows. The code is based on an Arbitrary Lagrangian–Eulerian (ALE) scheme as described by Hirt et al.[64] The name refers to the flexibility of the scheme, which allows for the mesh either to be moved along with the fluid (Lagrangian), to remain in a fixed position (Eulerian), or to be moved in another fashion as selected by the user. The ALE scheme is designed to handle flows at any speed, including the limiting cases of fully incompressible flow and hypersonic flow, and it allows for multifluid and multiphase calculations for an arbitrary number of fluid fields. Kashiwa et al.[62,63] state that the numerical method is a generalization of the implicit continuous-fluid Eulerian (ICE) scheme proposed by Harlow and Amsden,[65] which is stable for any value of the Courant number based on the speed of sound. Additionally, Kashiwa et al.[62,63] state that the ICE method in effect becomes identical to the Marker and Cell (MAC) method for the limiting case of incompressible flow considered in this work.

The computational cycle is executed repeatedly as the time-dependent state proceeds in increments of Δt. This cycle is composed of three parts: (1) the primary phase, which accounts for the calculation of auxiliary quantities; (2) the Lagrangian phase, which accounts for the calculation of the effects of physical processes; and (3) the Eulerian phase, in which each state is remapped to a common control volume. All state quantities are considered to be cell-centered because this method uses only one control volume for all the elements of the state vector. Further details on the numerics can be found elsewhere.[62,63]

Governing equations

In this work, a Eulerian two-fluid model is used to simulate incompressible, unsteady flow in bubble columns. Mass transfer between the phases and bubble coalescence is not considered. For two-phase flow the general forms of the equations[60] are given below. Subscript c refers to the continuous (liquid) phase and subscript d refers to the dispersed (bubble) phase.

The mass balance equation for phase k $(=c, d)$ is expressed as

$$\frac{\partial \alpha_k \rho_k}{\partial t} + \nabla \cdot (\alpha_k \rho_k \boldsymbol{u}_k) = 0 \tag{1}$$

The momentum balance equation for phase k is given by

$$\alpha_k \rho_k \frac{\partial \boldsymbol{u}_k}{\partial t} + \alpha_k \rho_k \boldsymbol{u}_k \cdot \boldsymbol{\nabla} \boldsymbol{u}_k = -\alpha_k \boldsymbol{\nabla} p + \boldsymbol{\nabla} P_k + \boldsymbol{\nabla} \cdot \alpha_k \mu_{eff,k} [\boldsymbol{\nabla} \boldsymbol{u}_k + (\boldsymbol{\nabla} \boldsymbol{u}_k)^T] + \sum_f \boldsymbol{F}_{fk} + \alpha_k \rho_k \boldsymbol{g} \tag{2}$$

The terms on the right-hand side of Eq. 2 represent, from left to right, the pressure gradient, bubble pressure, effective stress, interfacial momentum exchange, and the gravitational force. In our work, the bubble-pressure term appears when the BP and BIT models are used. For laminar flow simulations, P_k is set equal to zero. Likewise, for the continuous phase, P_c is set to zero. The closures for bubble pressure, effective stress, and interfacial momentum exchange are discussed below.

Note that the phase densities ρ_c and ρ_d are assumed to be constant in this work. Thus, because $\alpha_c + \alpha_d = 1$, the phase-average velocity ($\boldsymbol{u}_v = \alpha_c \boldsymbol{u}_c + \alpha_d \boldsymbol{u}_d$) is solenoidal: $\boldsymbol{\nabla} \cdot \boldsymbol{u}_v = 0$. This fact can be used to find the governing equation for the pressure p from Eq. 2.[62,63] Note also that both phases are assumed to share the same pressure p in Eq. 2. In a recent review, Sokolichin et al.[7] argue that gas–liquid flows can be adequately described by a simplified version of the two-fluid model. We choose not to follow their approach and instead solve the complete two-fluid model with all relevant force terms. In doing so, we are able to show that certain terms that are assumed negligible in deriving the simplified model play a key role in stabilizing the homogeneous solution to the complete two-fluid model, and thus should not be neglected.

Bubble-pressure (BP) model

The BP model represents the transport of momentum arising from bubble-velocity fluctuations, collisions, and hydrodynamic interactions. Although this assumption is not supported by our results, the BP model is assumed in the literature to play an important role in bubble-phase stability.[66] The bubble-phase pressure consists of kinetic, collisional, and hydrodynamic contributions. The fluctuations in the bubble motion give rise to the kinetic contribution. The collisional contribution arises from collisions between the bubbles. The hydrodynamic contribution arises as a result of the relative motion of the bubbles and the spatial and velocity distribution of the bubbles.[66]

According to a study performed by Spelt and Sangani,[66] as α_d increases from zero, the bubble-phase pressure will increase from zero, arrive at a maximum value, and then decrease. Consequently, for suitably small values of α_d, the value of $dP_d/d\alpha_d$ is both positive and proportional to slip velocity and holdup, and the collisional and hydrodynamic contributions are not considered. This results in the following expression for the bubble-phase pressure

$$P_d = \rho_c C_{BP} \alpha_d (\boldsymbol{u}_d - \boldsymbol{u}_c) \cdot (\boldsymbol{u}_d - \boldsymbol{u}_c) \tag{3}$$

A positive value of $dP_d/d\alpha_d$ acts as a driving force for bubbles to move from areas of higher α_d to areas of lower α_d. This facilitates stabilization of the bubbly-flow regime. However, as α_d increases, the collisional and the hydrodynamic contributions become important.[67]

Biesheuvel and Gorissen[59] proposed a BP model of the following form

$$P_d = \rho_c C_{BP} \alpha_d (\boldsymbol{u}_d - \boldsymbol{u}_c) \cdot (\boldsymbol{u}_d - \boldsymbol{u}_c) H(\alpha_d) \tag{4}$$

where[68]

$$H(\alpha_d) = \left(\frac{\alpha_d}{\alpha_{dcp}}\right)\left(1 - \frac{\alpha_d}{\alpha_{dcp}}\right) \tag{5}$$

In Eq. 4, C_{BP} is the virtual-mass coefficient of an isolated bubble (0.5 for spherical bubbles) and α_{dcp} in Eq. 5 is the gas void fraction at close packing (set equal to 1.0 for our simulations). The closures given by Eqs. 3 and 4 state that P_d approaches zero as α_d approaches zero. However, Eq. 3 suggests that $dP_d/d\alpha_d$ continues to be nonzero as α_d approaches zero, whereas Eq. 4 suggests that $dP_d/d\alpha_d$ approaches zero as α_d approaches zero.[67] For this reason, we use Eq. 4 to represent the bubble pressure in our simulations. Nevertheless, Eq. 3 was also implemented and the results were found to be very similar to Eq. 4. This would appear unexpected in the case of small α_d; however, as noted in the Results and Discussion section, changes to the BP model did not significantly alter the flow profiles observed.

Effective viscosity

As the gas bubbles ascend through the column, their potential energy is converted into kinetic energy. The difference between the kinetic and potential energy is passed to the liquid phase through the interface. However, some fraction of the energy is dissipated at the gas–liquid interface, and the remaining energy goes to the liquid phase, where it is finally dissipated at very small scales in the wakes of the bubbles. Various models have been proposed to account for this "bubble-induced turbulence" (BIT).[7] Sato and Sekoguchi[43] proposed a BIT model proportional to the bubble diameter and slip velocity of the rising bubbles

$$\mu_{t,c} = \rho_c C_{BT} \alpha_d d_b |\boldsymbol{u}_d - \boldsymbol{u}_c| \tag{6}$$

where the value of the proportionality constant C_{BT} is 0.6.[69] Sato's BIT model yields an effective viscosity in the liquid (continuous) phase. Thus, the effective viscosity term ($\mu_{eff,c}$) for the *continuous*-phase momentum balance (Eq. 2) is the sum of the molecular viscosity of the continuous phase and the turbulent viscosity calculated from the BIT model

$$\mu_{eff,c} = \mu_{0,c} + \mu_{t,c} \tag{7}$$

whereas the effective viscosity for the *dispersed* phase ($\mu_{eff,d}$) is assumed equal to the molecular viscosity of the dispersed phase. Finally, it should be noted that if the BIT model is enabled, it is assumed to work together with the BP model (Eq. 4) discussed previously.

Pan et al.[26] included Sato's BIT model in their simulations. Deen et al.[35] performed simulations on square cross-sectioned bubble columns using LES combined with the BIT model, and the k–ε model combined with the BIT model. However, they observed only a marginal difference between the simulations with and without the BIT model. Troshko and Hassan[70] applied Sato's BIT model for bubbly flow in a pipe and compared the turbulent intensity in the bubbly flow with single-phase flow. They observed that Sato's BIT model enhanced turbulence, and attributed the increase to the pseudo-turbulence caused by the wakes of bubbles. Buscaglia et al.[16] noted, however, that corrections to the k–ε model to account for bubble-induced turbulence are insignificant.

The turbulent viscosity can also be described by other turbulence-modeling approaches, such as the family of k–ε models or LES.[7] It should be noted that the k–ε model available in CFDLib calculates the turbulence generated at the gas–liquid interface in the form of a slip-production energy term.[71] We have tested this model for the homogeneous flow cases presented in the Results and Discussion section and found that the results are in disagreement with the experiments discussed in the section on column flow regimes. As noted in the introduction, this result is not unexpected, given that the liquid phase is nearly laminar in the homogeneous flow regime. Therefore, because of the generally poor quality of the flow predictions, we do not report simulation results using the k–ε model for the flow conditions considered in this work.

Interfacial momentum exchange

The interfacial momentum exchange accounts for the interaction between the continuous and the dispersed phases, which is caused by local variations in pressure and stress. These variations occur when liquid flows around a bubble, resulting in a relative motion between individual bubbles and the surrounding liquid.[72] The total interfacial force acting on either of the phases is given by a sum of the individual forces

$$\sum_f \boldsymbol{F}_{fk} = \boldsymbol{F}_{D,k} + \boldsymbol{F}_{rot,k} + \boldsymbol{F}_{L,k} + \boldsymbol{F}_{vm,k} + \boldsymbol{F}_{S,k} \tag{8}$$

It should be noted that Eq. 8 is presented as it would appear in the momentum balance for the dispersed phase. The opposite sign would be used when considering Eq. 8 for the continuous phase. For example, $\boldsymbol{F}_{D,d} = -\boldsymbol{F}_{D,c} = \boldsymbol{F}_D$.

The formulation of the drag force is a key issue in multiphase flows. Clift et al.[72] and Joshi et al.[73] have given excellent accounts of this subject. The drag force is felt on a swarm of equal-sized bubbles as they travel steadily through a fluid, and is defined in CFDLib as

$$\boldsymbol{F}_D = -\alpha_d \alpha_c \rho_c C_D(\mathrm{Re}) \frac{3}{4d_b} |\boldsymbol{u}_d - \boldsymbol{u}_c|(\boldsymbol{u}_d - \boldsymbol{u}_c) \tag{9}$$

where Re denotes the bubble Reynolds number

$$\mathrm{Re} = \frac{d_b |\boldsymbol{u}_d - \boldsymbol{u}_c|}{\nu_c} \tag{10}$$

The drag coefficient is a function of the bubble Reynolds number, and there are various functional relationships available in the literature.[3,5,7] CFDLib uses the drag relation expressed by[62,63]

$$C_D(\mathrm{Re}) = 0.5 + \frac{24}{\mathrm{Re}} + \frac{6}{1 + \sqrt{\mathrm{Re}}} \tag{11}$$

However, results found with other correlations differ primarily in the dependency of the volume-averaged gas holdup on the bubble diameter. For example, Sankaranarayanan et al.[74] developed a closure dependent on holdup, bubble Reynolds number, Eötvös number, and Morton number. Their closure model is applicable for both hindered rise and cooperative rise, is valid for $0 < \alpha_d < 0.2$, and is restricted to bubbles in cubic arrays.

We have found that instantaneous flow-field predictions for all drag-force models are similar, provided that no additional dependency on α_d is added to Eq. 9. For example, if a power-law dependency on bubble volume fraction is introduced in Eq. 9 to account for bubble–bubble interactions, we find that adding other force models cannot stabilize the instantaneous flow field. Similar conclusions concerning flow instability induced by holdup-dependent drag-force models have been reported by others.[34]

The drag force accounts for the interaction between gas and liquid under nonaccelerating conditions. Once a bubble accelerates, an additional force contribution, known as the added-mass or virtual-mass force, must be considered.[60] The virtual-mass force is exerted on a moving bubble when it accelerates and in turn accelerates the surrounding fluid[60]

$$\boldsymbol{F}_{vm} = -\alpha_d\alpha_c\rho_v C_{vm}\left[\left(\frac{\partial \boldsymbol{u}_d}{\partial t} + \boldsymbol{u}_d \cdot \nabla \boldsymbol{u}_d\right) - \left(\frac{\partial \boldsymbol{u}_c}{\partial t} + \boldsymbol{u}_c \cdot \nabla \boldsymbol{u}_c\right)\right] \tag{12}$$

where ρ_v denotes the volumetric density:

$$\rho_v = \alpha_c\rho_c + \alpha_d\rho_d \tag{13}$$

The virtual-mass coefficient C_{vm} is generally shape dependent. Drew et al.[75] used 0.5 for rigid spherical particles, whereas Cook and Harlow[76] used 0.25 for bubbles in water. The coefficient has also been assumed to be a function of holdup, as suggested by Homsy et al.[77] and Biesheuvel and Spoelstra.[78] In the present work, the virtual-mass coefficient is assumed to be 0.5, which is the value for dilute suspensions of spheres in a fluid.[60] Sankaranarayanan et al.[74] developed a model for the virtual-mass coefficient, and observed that C_{vm} increased nearly linearly with increasing α_d, for both spherical and distorted bubbles. Additionally, they found a correlation between C_{vm} for isolated bubbles and the aspect ratio of isolated bubbles.

It should be noted that Hunt et al.[79] suggested that for bubble columns in which the diameter is $\gtrsim$15 cm, the effect of the virtual-mass force is negligible. In such columns, the square of the terminal rise velocity would be smaller than the product of the gravitational constant and the characteristic length scale, and the drag force would dominate the interface coupling term. However, Delnoij et al.[22] noted that including the virtual-mass force prevents bubbles from accelerating at unrealistically high rates. Indeed, in this work we find that the virtual-mass force plays an important role in stabilizing homogeneous flow, and thus that it cannot be neglected for large columns.

A bubble traveling through a fluid in shearing motion will experience a lift force transverse to the direction of motion.[60] This force depends on the vorticity of the continuous phase. For a spherical bubble, the lift force is given by[60]

$$\boldsymbol{F}_L = \alpha_d\alpha_c\rho_v C_L(\boldsymbol{u}_d - \boldsymbol{u}_c) \times \nabla \times \boldsymbol{u}_c \tag{14}$$

Discussion by Drew and Passman[60] with respect to the constitutive equations for multiphase flow also includes a term proportional to $(\boldsymbol{u}_d - \boldsymbol{u}_c) \times \nabla \times \boldsymbol{u}_d$. Thus, the rotation force, which depends on the vorticity of the dispersed phase, is also included in the interfacial momentum exchange[60]

$$\boldsymbol{F}_{rot} = \alpha_d\alpha_c\rho_v C_{rot}(\boldsymbol{u}_d - \boldsymbol{u}_c) \times \nabla \times \boldsymbol{u}_d \tag{15}$$

It should be noted that CFDLib assigns equal values to the lift coefficient C_L and the rotation coefficient C_{rot}. (Refer to Appendix A for further details.)

Arnold et al.[80] suggest that gradients within the dispersed phase have a significant effect on the direction and magnitude of the interfacial force. Clift et al.[72] stated that particles or fluids can rotate about axes either normal or parallel to the direction of relative motion. The former case is known as top spin, when rotation is caused by fluid shear or collisions. A basic example considers a nearly spherical object, such as a bubble or particle, in a uniform shear flow field in the plane of the object (here, the x–y plane). The center of the object will move with the velocity that the continuous fluid would have at that same location if no object was present. Meanwhile, the axis of the object will experience rotation in a periodic path, in which the angular velocities depend on the angle between the object's axis of symmetry and the z-axis, the angle between the y–z plane and the plane containing both the z-axis and the object's axis of symmetry, the shear rate, and the shape of the object.[72] Rotation about axes parallel to the direction of relative motion is called screw motion, which is characterized by the Reynolds number and the ratio of surface speed to approach velocity. Bubbles experiencing screw motion tend to become flatter as the angular velocity increases.[72]

There has been considerable debate regarding the appropriate value of the lift coefficient C_L, and the significance of the lift force in simulations. Delnoij et al.[22] stated that including the lift force in Eulerian–Lagrangian models is necessary for the realistic representation of flow behavior in bubble columns. Auton[81] showed that the lift coefficient C_L has a value of 0.5. This value has also been reported in more recent studies, including Deen et al.,[35] Lain et al.,[6] and Bove et al.[36] However, Drew and Passman[60] suggest using $C_L = C_{rot} = 0.25$ if $C_{vm} = 0.5$. Their thorough description of frame indifference and objectivity for the two-fluid model shows that if $C_L + C_{rot} = C_{vm}$, then the principle of objectivity is satisfied. Additionally, Drew and Passman[60] state that if $C_L = C_{rot} = 0.5\ C_{vm}$, then the sum $\boldsymbol{F}_{vm} + \boldsymbol{F}_L + \boldsymbol{F}_{rot}$ is frame indifferent.

Tomiyama et al.[82] determined an empirical correlation for a net transverse lift coefficient, where for $d_b < 4.4$ mm, C_L was found to be a function of the bubble Reynolds number, whereas for $d_b > 4.4$ mm, C_L was found to be a function of a modified Eötvös number, where the characteristic length used was the maximum horizontal dimension of the bubble. The sign of C_L changed from positive to negative when $d_b = 5.8$ mm. Tomiyama et al.[82] suggested three possible regimes for lateral bubble movement in a vertical pipe: (1) the wall regime (0.4 mm $< d_b <$ 5 mm), in which C_L has a large positive value and bubbles move toward the wall; (2) the core regime ($d_b >$ 6 mm), in which C_L has a large negative value and bubbles move toward the center of the pipe; and (3) a neutral regime ($d_b <$ 0.4 mm; 5 mm $< d_b <$ 6 mm), in which C_L has a small magnitude and bubble movement is influenced by factors such as turbulence or bubble residence time. Sankaranarayanan and Sundaresan[67] developed a closure for the lift force, valid for $Ca_\gamma < 0.01$ and $\alpha_d < 0.15$, where Ca_γ is the capillary number based on dimensionless shear rate. They observed that for $Ca_\gamma < 0.01$, the lateral drift velocity exhibited a linear relationship with Ca_γ. As Ca_γ was increased, the relationship eventually became nonlinear and C_L became a function of Ca_γ. It was also observed that C_L gradually decreases with increasing Ca_γ, and that the sign of C_L would change from positive to negative when $Ca_\gamma \cong 10^{-1}$. However, Sankaranarayanan and Sundaresan[67] noted that for air–water systems in which 1 mm $< d_b <$ 10 mm, $Ca_\gamma \cong 10^{-3}$–10^{-2}. Therefore, C_L was expected to remain positive for bubble column flows. Such disagreement regarding the lift force led Sokolichin et al.[7] to question the significance of this force in bubble-column simulations. Our work, however, clearly demonstrates the importance of the lift force to the stability of homogeneous flow predictions of the two-fluid model.

Finally, CFDLib contains a strain force that is also applied in our calculations, expressed as

$$\boldsymbol{F}_S = \alpha_d \alpha_c \rho_v C_S [(\nabla \boldsymbol{u}_c + \nabla \boldsymbol{u}_d) + (\nabla \boldsymbol{u}_c + \nabla \boldsymbol{u}_d)^T] \cdot (\boldsymbol{u}_c - \boldsymbol{u}_d) \tag{16}$$

To our knowledge, the strain force developed by Kashiwa[83] does not appear in gas–liquid flows previously discussed in the literature. Nevertheless, we have studied its effect on flow stability in our earlier work.[37] Appendix A provides further details regarding the representation of the lift, rotation, and strain forces in CFDLib. In this work, positive values are used for the lift and rotation coefficients. Appendix B demonstrates how the equations in the two-fluid model can be made dimensionless.

It should be noted that the standard definitions of the virtual-mass, lift, and rotation forces[60] differ slightly from the models applied in CFDLib. When these forces are modeled in CFDLib, the volume fractions for both phases are included, instead of the volume fraction of the dispersed phase only (cf. Eqs. 12, 14, and 15). In addition, CFDLib uses the volumetric density (Eq. 13) instead of using the density for the continuous phase. These definitions ensure that the model equations treat each phase in an analogous manner at very high and very low bubble volume fractions. It may also be noted that the liquid density (1 g/cm^3) is much larger than the gas density (0.001 g/cm^3); therefore, the volumetric density is close to the liquid density.

Results and Discussion

The first set of simulations is based on experiments using small-diameter columns, performed by Garnier et al.,[56,57] but with slight differences from their experimental setup described previously. Unless stated otherwise, the simulations are performed on a 2-D Cartesian grid with free-slip boundary conditions at the column walls. Additionally, the column height is extended to 50 cm to provide sufficient freeboard at the top of the column. The column is initially filled with water, and uniform aeration is turned on at the beginning of the simulations. After several seconds of real time, the simulations reach a statistically steady-state flow regime. All results presented are taken for flows in this regime. Table 2 summarizes the conditions for all simulations reported in this work. It should be noted that in some simulations the bubble diameter is held constant at the value reported in the experiments. In other cases, simulations are run for different bubble diameters to determine their effect on the flow predictions. Also note that changing the bubble diameter corresponds to changing the bubble Reynolds number. In this work we consider bubble Reynolds numbers in the range $25 \leq \mathrm{Re} \leq 1100$. In all cases, bubble coalescence is neglected and the physical properties of air and water at room temperature are used.

Our numerical results are divided into the following categories. First, commentary on the effect of the wall boundary conditions is given. Then, the effect of grid resolution on laminar-flow simulations is discussed. Next, the effects of force-model parameters on both laminar-flow simulations and simulations applying the BIT model are presented for the homogeneous flow regime. Then, the combined effect of force-model parameters and the BIT model on transitional-flow behavior in 6-cm columns is studied. Subsequently, for high-flow-rate simulations both the effect of bubble size on flow structures and the effect of liquid coflow on the flow stability are discussed. Finally, flow predictions for scale-up in terms of column diameter are analyzed.

Effect of wall boundary conditions

The two types of wall boundary conditions considered for our numerical studies are free-slip, for which velocity gradients at the wall are assumed to be null, and periodic, for which a pseudo-infinite domain is assumed. As shown in Figure 3, the use of periodic boundary conditions results in unphysical bands in the velocity vector fields for laminar-flow simulations and for cases in which small bubble diameters ($d_b \approx$ 0.5 mm) are considered. Figure 3 illustrates this phenomenon for a 6-cm column using an air inlet flow rate of 2 cm/s with d_b set to 0.5 mm (Figure 3, left) and an air inlet flow rate of 12 cm/s with d_b again set to 0.5 mm (Figure 3, right). The unphysical velocity bands are not observed for simulations using free-slip boundary conditions. For this reason, the majority of the simulations discussed in the present work are performed with free-slip boundary conditions at the column walls. It is interesting to observe that when the gas phase is introduced as a point source (instead of uniformly) in bubble-column experiments, meandering plumes are observed.[7] We can thus speculate that the wavelength of the banded velocity structures seen with periodic walls will be related to the meandering frequency found in simulations with nonuniform inlet boundary conditions.[28]

It should be noted that the presence of velocity bands is dependent on the flow domain used. For example, we have observed that the use of periodic boundary conditions for a flow domain of 256 × 256 cm^2 generates recirculation cells separated by approximately 100–150 cm, instead of bands. This suggests that the liquid level most likely determines the recirculation-cell spacing. Additionally, recirculation cells are found with 2-D periodic boundary conditions when the flow-domain width is larger than the liquid level, suggesting that periodic boundary conditions should not be used for cases with large height/width ratios. Finally, we note that the appearance of banded velocity fields is neither unique to air–water bubble columns nor an artifact of our simulation code. We have observed analogous banded structures when simulating gas–solid fluidized beds with other two-fluid simulation codes that use very different numerics. Moreover, we find that they are very robust and do not depend on the details of force models or grid resolution. We can thus speculate that banded velocity fields are a generic property of the two-fluid model equations for 2-D periodic domains. Although we have not done so yet,

Table 2. Summary of Conditions for Numerical Simulations

General Simulation Conditions	
Column height	50 cm
Grid Resolution	
Column width	6 cm
Bubble diameter	4 mm
Inlet velocities	Air: 2 cm/s, Water: 1.6 cm/s
(C_{vm}, C_L, C_{rot}, C_S)	(0.5, 0.75, 0.75, 0.25)
Vertical boundary conditions	Free-slip
Homogeneous Flow	
Column width	6 cm
Inlet velocities	Air: 2 cm/s, Water: 0 cm/s
(C_{vm}, C_L, C_{rot}, C_S)	(0.5, 0.75, 0.75, 0.25); (0.5, 0.375, 0.375, 0.125); or (0, 0, 0, 0)
Vertical boundary conditions	Free-slip: all cases; Periodic: (C_{vm}, C_L, C_{rot}, C_S) = (0.5, 0.375, 0.375, 0.125) only
Transitional Flow	
Column width	6 cm
Bubble diameter	4 mm
Inlet velocities	Air: 2, 6.2, and 12 cm/s; Water: 1.6 cm/s
(C_{vm}, C_L, C_{rot}, C_S)	(0.5, 0.75, 0.75, 0.25); (0.5, 0.375, 0.375, 0.125); or (0, 0, 0, 0)
Vertical boundary conditions	Free-slip: all cases; Periodic: (C_{vm}, C_L, C_{rot}, C_S) = (0.5, 0.375, 0.375, 0.125) only
Effect of Bubble Size on Flow Structures	
Column width	6 cm
Inlet velocities	Air: 12 cm/s, Water: 1.6 cm/s
(C_{vm}, C_L, C_{rot}, C_S)	(0.5, 0.375, 0.375, 0.125)
Vertical boundary conditions	Free-slip and periodic
Effect of Liquid Coflow	
Column width	6 cm
Bubble diameter	4 mm
Inlet velocities	Air: 12 cm/s, Water: 0, 1.6, and 3.3 cm/s
(C_{vm}, C_L, C_{rot}, C_S)	(0.5, 0.375, 0.375, 0.125)
Vertical boundary conditions	Free-slip
Effect of Column Diameter (Homogeneous Flow)	
Column width	6, 20, 40 cm
Inlet velocities	Air: 2 cm/s, Water: 0 cm/s
(C_{vm}, C_L, C_{rot}, C_S)	(0.5, 0.75, 0.75, 0.25); (0.5, 0.375, 0.375, 0.125); or (0, 0, 0, 0)
Vertical boundary conditions	Free-slip
Effect of Column Diameter (Transitional Flow)	
Column width	6, 40 cm
Bubble diameter	4 mm
Inlet velocities, transitional flow	Air: 2 and 12 cm/s; Water: 1.6 cm/s
(C_{vm}, C_L, C_{rot}, C_S)	(0.5, 0.375, 0.375, 0.125)
Vertical boundary conditions	Free-slip

it would be interesting to simulate a 3-D periodic domain with a square cross section for which no preferential direction is present. Because of symmetry, banded velocity fields for this case would not be expected.

Grid resolution

As shown in our earlier work,[37] domain size and grid resolution have a significant effect on flow simulations. In the present case, grid-resolution studies were carried out for a 6-cm column using 2-D and 3-D grids. Figure 4 illustrates typical water volume-fraction profiles at different grid resolutions. The simulations were performed using an air inflow rate of 2 cm/s and a water inflow rate of 1.6 cm/s. Figure 4A shows that a coarse grid (albeit typical of previous studies; see Table 1) results in a near homogeneous flow pattern without any flow structures. Such behavior is caused by numerical diffusion, which smooths out velocity and volume-fraction gradients on coarse grids. Sokolichin and Eigenberger[24] reported similar effects of numerical diffusion.

With a refined grid of 0.25 cm (Figure 4B), large-scale plume structures are obtained and persist throughout nearly the entire column length. Further grid refinement to 0.1 cm (Figure 4C) shows vertical plumes of even finer scale, primarily at the bottom of the column. At a height between 25 and 30 cm, these plumes break up into smaller structures. Similar structures have been observed in gas–solid flow simulations using the two-fluid model.[38] One can safely assume that further grid refinement will result in even finer structures. Monahan and Fox[37] observed such behavior, and also found that the flow structures depend on the force models used. However, it is also worth noting that such fine grids may be impractical for simulating industrial-scale bubble columns. In this case, subgrid models would be needed to perform large-eddy simulations of industrial bubble columns.[38]

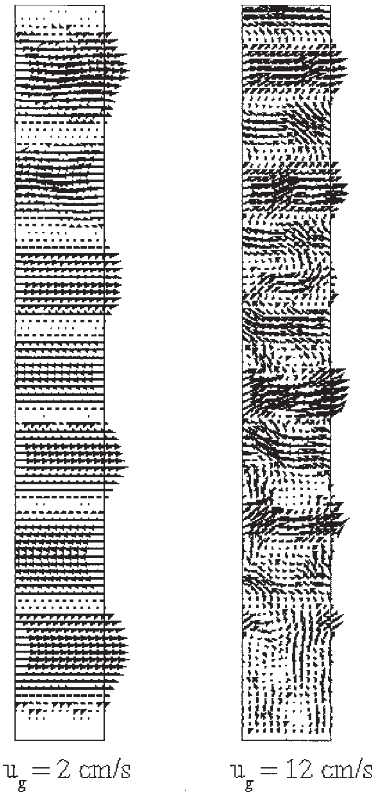

Figure 3. Water velocity vector fields for simulations using periodic boundary conditions.

Left: Inlet air velocity of 2 cm/s. Right: Inlet air velocity of 12 cm/s. The horizontal bands are unphysical, and observed only with periodic boundary conditions.

To justify the use of a 2-D grid, 3-D simulations were carried out on a grid using 0.25-cm spacing. Figure 4D shows a 2-D slice of the 3-D domain. It can be seen that these 3-D flow structures are comparable to those shown in Figure 4B. Furthermore, no significant change in the volume-averaged gas holdup was observed when using either a more refined grid or a 3-D domain, both of which greatly increase the computational cost. Thus, unless otherwise noted, all further simulations reported in this work are performed on 2-D domains using a 0.25-cm grid. Finally, it should be noted that when refined grids are used (Figure 4C), the laminar two-fluid model does not predict the homogeneous-flow regime expected for the air inflow rate used (2 cm/s). Thus, the next step in our investigation is to examine what additional terms are needed in the two-fluid model to predict homogeneous flow on refined grids.

Homogeneous flow

According to the flow-regime map shown in Figure 1, a 6-cm-wide column with 2 cm/s inlet air velocity should operate in the homogeneous-flow regime. Initially, the BP model (Eq. 4) was incorporated into the two-fluid model in an attempt to obtain homogeneous flow. As discussed previously, the BP model should help to maintain the uniform-bubbling state by driving the bubbles from higher- to lower-holdup regions. To study the sensitivity of the model (Eq. 4), C_{BP} was set to 0.2, 0.5, and 1.0. (The virtual-mass coefficient C_{vm} remained 0.5 for all other calculations during these simulations.) Although the flow dynamics changed slightly, no significant effect of the BP model on the holdup distribution was observed. C_{BP} was set equal to 0.2 for all subsequent simulations. Nevertheless, simulations with C_{BP} set equal to zero are qualitatively identical to the results presented in this work.

As noted in the introduction, bubble wakes result in enhanced turbulence in the liquid phase. Thus, to reduce the circulation and vortical structures observed in the laminar-flow simulations (that is, $\mu_{eff,c} = \mu_{0,c}$), the BIT model (Eq. 6) was introduced and tested. As mentioned previously, the BIT model is assumed to work together with the BP model. However, it was determined that the addition of the BIT model alone (with or without the BP model) is not sufficient to generate homogeneous flow on refined grids.

In the next step, a study of the force models and parameter values was undertaken to determine whether the two-fluid model could produce homogeneous flow. This study was carried out for 6-cm columns with an air inflow rate of 2 cm/s and a water inflow rate of 0 cm/s. The value for the bubble diameter was varied from 0.5 to 4 mm, corresponding to bubble Reynolds numbers of approximately 25 and 1100, respectively. Both laminar-flow simulations ($\mu_{eff,c} = \mu_{0,c}$), and simulations applying the BIT model, were performed for several bubble diameter (or Reynolds number) values in this range. Three main force model combinations were considered:

(1) All forces (virtual mass, drag, lift, rotation, and strain) enabled with the nominal coefficient values. The virtual-mass coefficient is equal to 0.5, the lift and rotation coefficients are equal to 0.75, and the strain coefficient is equal to 0.25. This is the same combination that was applied toward the laminar-flow grid-resolution study.

(2) All forces enabled with the virtual-mass coefficient equal to 0.5. The lift and rotation coefficients are equal to 0.375, and the strain coefficient is equal to 0.125 (that is, half the nominal values).

(3) Only drag force enabled, where the virtual-mass, lift, rotation, and strain coefficients are all equal to zero.

Table 2 summarizes the conditions for these simulations.

A quantitative analysis of the simulation results can be performed by plotting the volume-averaged gas holdup ($\bar{\alpha}_d$) and the volume-averaged slip velocity ($\bar{U}_S$) as functions of the bubble diameter (d_b), and the holdup fluctuations (σ) and slip-velocity fluctuations (θ) as functions of the bubble Reynolds number Re (see Figures 5 and 6). The volume-averaged quantities are obtained by taking an average over all the nodes in the calculation domain at the final time step of the simulation. It should be noted that determining the values for $\bar{U}_S$ is required to calculate the values of Re. Studying the deviations from these averaged quantities allows further insight into the stability of the flow. Smaller values for σ and θ indicate higher stability, or a tendency toward homogeneous flow (that is, the deviations from the volume-averaged quantities are small). The expressions for σ and θ are given by

$$\sigma = \frac{\sqrt{\overline{\alpha'_d \alpha'_d}}}{\bar{\alpha}_d} \qquad \theta = \frac{\sqrt{\overline{U'_S U'_S}}}{\bar{U}_S} \tag{17}$$

where $\alpha'_d = \alpha_d - \bar{\alpha}_d$ and $U'_S = U_S - \bar{U}_S$. Values of σ and θ are calculated in the following manner. First, the local devia-

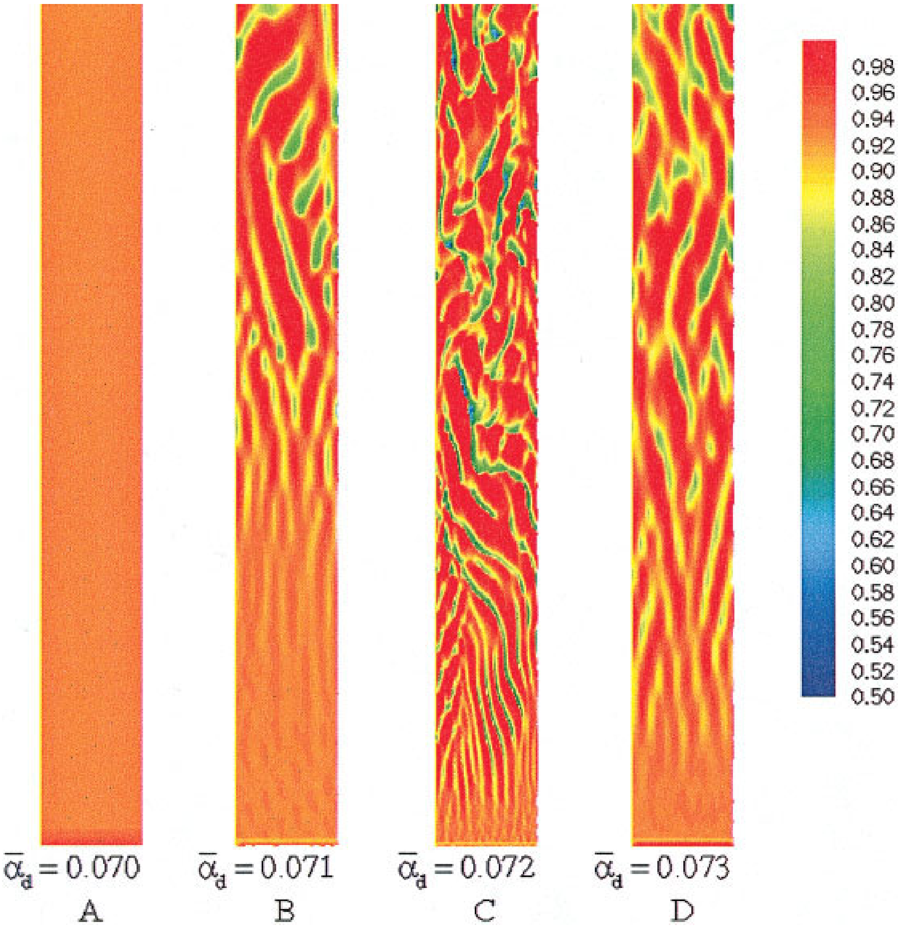

Figure 4. Water volume-fraction profiles for different grid sizes.

(A) 2-D, 1 cm. (B) 2-D, 0.25 cm. (C) 2-D, 0.10 cm. (D) 3-D, 0.25 cm. Volume-averaged gas holdup ($\bar{\alpha}_d$) is shown at the bottom of each profile.

tion values, α'_d and U'_S, are determined by subtracting the volume-averaged value from the local value for each node in the domain. Then each local deviation value is squared and an average of these squares is taken over the domain. The square root of this average is finally divided by the volume-averaged mean. (For our purposes, $U_S = u_{d,y} - u_{c,y}$.)

Figure 5 presents the quantitative analysis for the 6-cm column using the laminar-flow model. It can be seen that when the laminar-flow model is applied, the line plots for the volume-averaged gas holdup and slip velocity are in agreement, regardless of the force models and parameter values used. Additionally, the fluctuation data for the laminar-flow simulations tend to be high, with the values of σ and θ increasing with increasing bubble Re. For nearly all bubble Re, enabling all force models with $C_{vm} = 0.5$, $C_L = C_{rot} = 0.375$, and $C_S = 0.125$ resulted in lower values of σ and θ than for the other force-model combinations, sometimes by nearly an order of magnitude. These results indicate that using $C_{vm} = 0.5$, $C_L = C_{rot} = 0.375$, and $C_S = 0.125$ is an improvement toward predicting homogeneous flow. However, even when these parameter values are used, the highest values of σ and θ observed are about 10^{-1} and 10^{-2}, respectively, indicating higher deviations from the average than we expected for homogeneous flow. Qualitatively, all laminar-flow simulations predict water volume-fraction profiles similar to Figure 4B.

Figure 6 presents the quantitative analysis for the 6-cm column with the BIT model. As seen for the case in which the laminar-flow model was used (Figure 5), the volume-averaged quantities are nearly equal regardless of force models enabled or parameter values used. However, it is clear from the plots for σ and θ that varying the force models enabled (or their coefficients) affects the flow stability. As the bubble Re decreases, the values for σ and θ for each simulation approach the limiting value observed in the laminar-flow simulations. This result is not unexpected because the BIT model is directly proportional to the bubble diameter, and thus has no effect at zero bubble diameter, or zero bubble Re. With the BIT model and all forces enabled with $C_L = C_{rot} = 0.75$ and $C_S = 0.25$, the values for σ and θ tend to decrease with increasing bubble Re until Re is approximately equal to 210, after which both σ and θ increase with increasing bubble Re. A similar trend is observed when $C_L = C_{rot} = 0.375$ and $C_S = 0.125$; however, the values of σ and θ are overall lower, sometimes by up to two orders of magnitude. The transition observed when Re $\approx$ 210 occurs because the viscous term becomes more influential than the combined effect of the force models when Re is greater than approximately 210.

The opposite trend is observed when only the BIT model and the drag force are enabled. Values of σ and θ increase with increasing bubble diameter until Re is equal to about 275, after

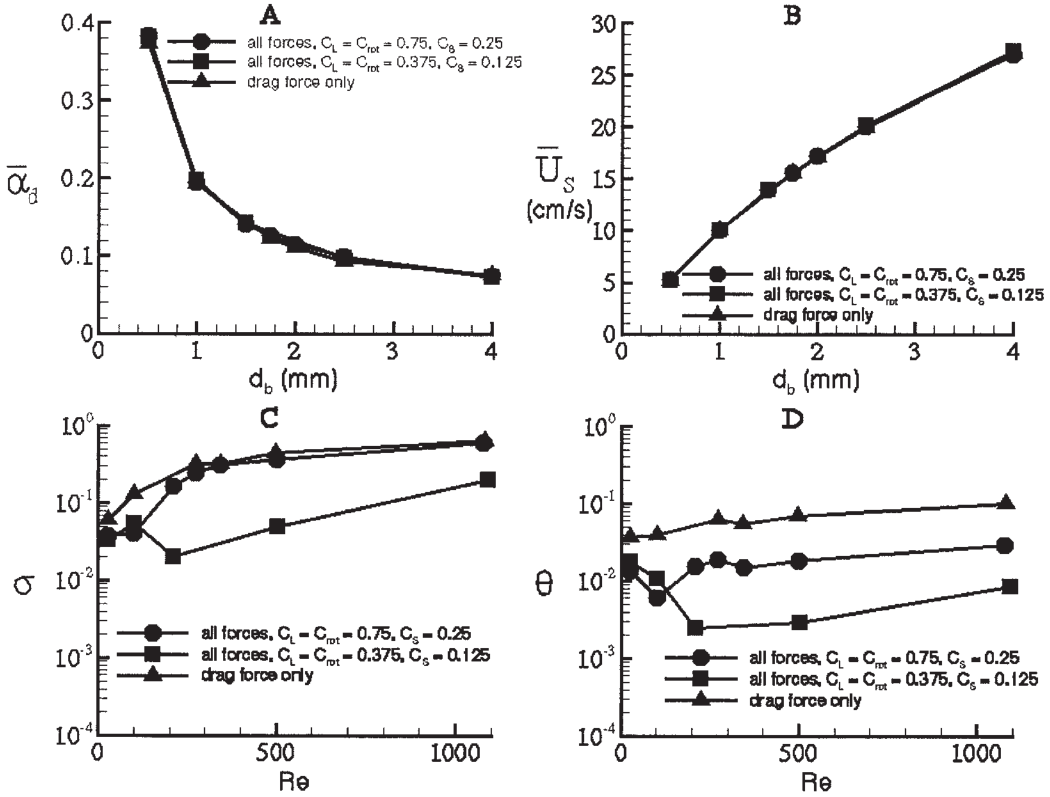

Figure 5. Quantitative analysis for a 6-cm column with the laminar-flow model.

(A) Volume-averaged holdup; (B) volume-averaged slip velocity; (C) holdup fluctuations; (D) slip-velocity fluctuations.

which both σ and θ decrease with increasing bubble Re. For Re values $\gtrsim 275$, the viscous term becomes of equal or greater influence when compared with the drag term, resulting in dampened fluctuations from average values. Additionally, for $\text{Re} > 275$, values of σ and θ are at least an order of magnitude lower than when the laminar model is used (Figure 5). Although simulations with the BIT model and virtual-mass and drag forces enabled were also performed (that is, with no lift, rotation, or strain), these were found to be numerically unstable and did not appear to follow a general trend. Therefore, such cases were not further investigated.

It should be noted that the case for which all forces are enabled, with $C_L = C_{rot} = 0.375$ and $C_S = 0.125$, was performed first with free-slip boundary conditions at the column walls, and then with periodic boundary conditions. Overall, as seen in Figure 6, the change in boundary conditions does not result in large differences in the quantitative analysis. However, the fluctuating quantities tend to be slightly smaller with periodic boundary conditions (most notably when $\text{Re} \approx 25$).

It may be noted that Deen et al.[35] did not observe any significant effect when using Sato's BIT model. On the other hand, Pfleger and Becker[28] observed a remarkable effect when considering bubble-induced turbulence by applying additional production terms in their k and ε equations. They observed a marked improvement on the simulation of radial profiles of axial velocities, but had less-successful predictions of local and overall gas holdup. The present work demonstrates that the use of the BIT model (Figure 6) generally results in lower values of σ and θ than when the laminar model is used (Figure 5). For this reason, all remaining simulations reported below use the BIT model to stabilize the flow.

Figures 5A and 6A, and Figures 5B and 6B, illustrate that the volume-averaged holdup and slip velocity, respectively, are determined by the drag coefficient alone, and are substantially independent of the instantaneous flow fields. Furthermore, because the drag model and its dependency on the bubble Reynolds number are inputs into the two-fluid model, comparisons of volume-averaged holdup and volume-averaged slip velocity with experimental data are of little use for validating the predictive abilities of two-fluid CFD models. In other words, changes in the force models can yield instantaneous flow fields that range from highly turbulent to nearly time invariant, but which have exactly the same average holdup and average slip velocity. It would appear from Figure 6 that including the BIT model, enabling all force models, and using $C_{vm} = 0.5$, $C_L = C_{rot} = 0.375$, and $C_S = 0.125$ are sufficient requirements for the two-fluid model to yield homogeneous-flow predictions.

Transitional flow

The next goal is to determine whether the two-fluid model, with the inclusion of the BIT model and parameter settings of $C_{vm} = 0.5$, $C_L = C_{rot} = 0.375$, and $C_S = 0.125$, will yield reasonable predictions for transitional-flow behavior in 6-cm columns. To do this, 2-D simulations are carried out for three inlet air velocities: 2, 6.2, and 12 cm/s. As in the experiments of Garnier et al.,[56,57] an inlet water velocity of 1.6 cm/s is used, and the bubble diameter is set to 4 mm ($\text{Re} \approx 1093$). Finally,

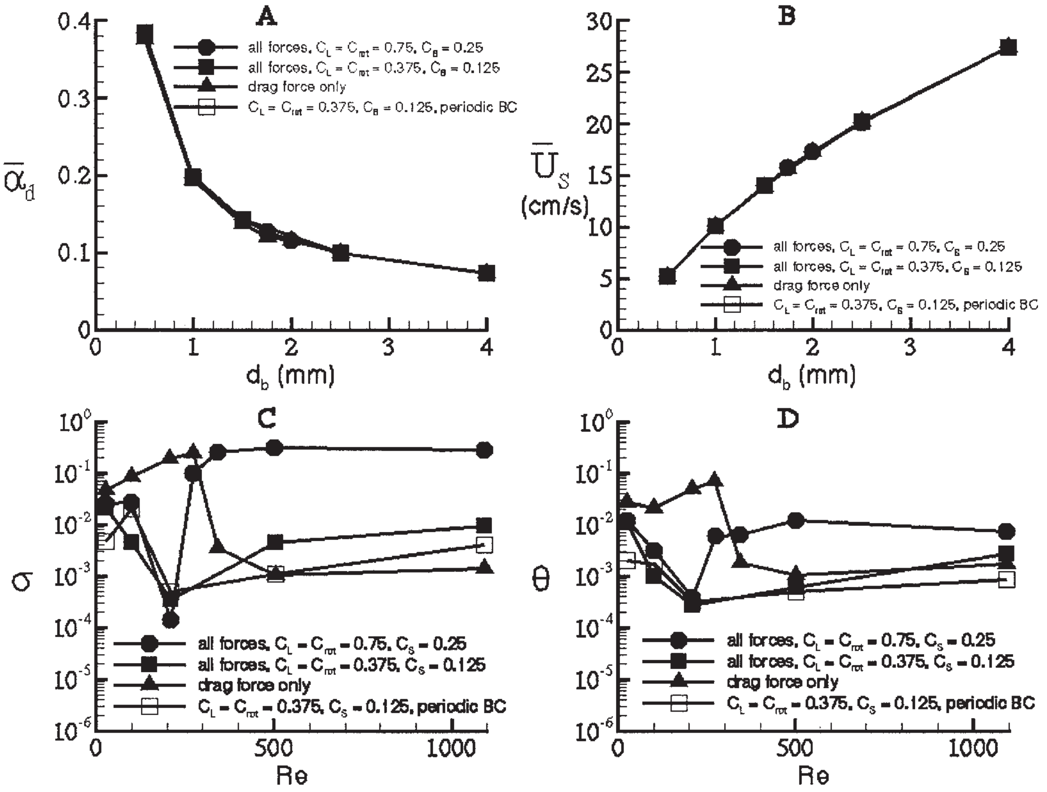

Figure 6. Quantitative analysis for a 6-cm column with the BIT model.

(A) Volume-averaged holdup; (B) volume-averaged slip velocity; (C) holdup fluctuations; (D) slip-velocity fluctuations.

as discussed previously, three main force models are studied: (1) all forces enabled, with $C_{vm} = 0.5$, $C_L = C_{rot} = 0.75$, and $C_S = 0.25$; (2) all forces enabled, with $C_{vm} = 0.5$, $C_L = C_{rot} = 0.375$, and $C_S = 0.125$; and (3) only drag force enabled, with $C_{vm} = C_L = C_{rot} = C_S = 0.0$. Conditions for these simulations are summarized in Table 2.

Figure 7 presents the quantitative analysis for transitional flow in 6-cm columns. The values for volume-averaged gas holdup ($\bar{\alpha}_d$), volume-averaged slip velocity ($\bar{U}_S$), holdup fluctuations (σ), and slip-velocity fluctuations (θ) are calculated in the same manner as previously described. However, for this study, $\bar{\alpha}_d$ and $\bar{U}_S$ are plotted as functions of inlet gas velocity u_g, and σ and θ are plotted as functions of $\bar{\alpha}_d$. It can be seen in Figures 7A and 7B that when all forces are enabled, the volume-averaged quantities are in agreement. However, the curve when only the drag force is enabled shows volume-averaged quantities that deviate from the other two curves at higher gas velocities. Only for the lowest inlet air velocity (2 cm/s) do all force-model combinations yield equal values for the volume-averaged quantities. It should be noted that, because a constant bubble diameter is used, the average slip velocity (and thus the bubble Reynolds number) does not change significantly with an increase in inlet air velocity. In other words, the gas flow rate controls $\bar{\alpha}_d$ and bubble diameter controls Re. Overall, the volume-averaged quantities are again insensitive to the instantaneous flow profiles occurring in the bubble column, and thus cannot be used to discriminate between different model formulations.

At high gas velocities, highly turbulent flow with irregular structures is expected from experiments.[61] Therefore, it would be expected that as the gas flow rate (and in turn $\bar{\alpha}_d$) increases, the values for σ and θ would also increase, indicating a tendency away from homogeneous flow. Such a trend is observed when only the drag force is enabled, and also when all forces were enabled with $C_L = C_{rot} = 0.375$ and $C_S = 0.125$ (Figures 7C and 7D). However, when all forces are enabled with $C_L = C_{rot} = 0.75$ and $C_S = 0.25$, the opposite trend is observed, that is, the lowest values of σ and θ are obtained for the highest value of $\bar{\alpha}_d$. (Note that a linear scale is used for σ in Figure 7C to highlight the transition from homogeneous to transitional flow.) The results for the force-model combination of $C_L = C_{rot} = 0.75$ and $C_S = 0.25$ are unexpected and viewed as an incorrect representation of transitional-flow behavior. When considering flow stability, it would appear that enabling all forces with $C_L = C_{rot} = 0.375$ and $C_S = 0.125$ yields the most reasonable representation of transitional flow in 6-cm columns. This model combination results in lower values for σ and θ than when only the drag force is enabled. This conclusion is further strengthened by a qualitative analysis of the water volume-fraction profiles.

Figures 8 and 9 provide this qualitative analysis of transitional-flow behavior by showing, respectively, the water volume-fraction profiles for the case in which only the drag force is enabled (Figure 8) and the case in which all forces are enabled with $C_L = C_{rot} = 0.375$ and $C_S = 0.125$ (Figure 9). According to the flow-regime map in Figure 1, for a 6-cm column, an inlet air velocity of 2 cm/s should result in a homogeneous-flow profile, an inlet air velocity of 6.2 cm/s

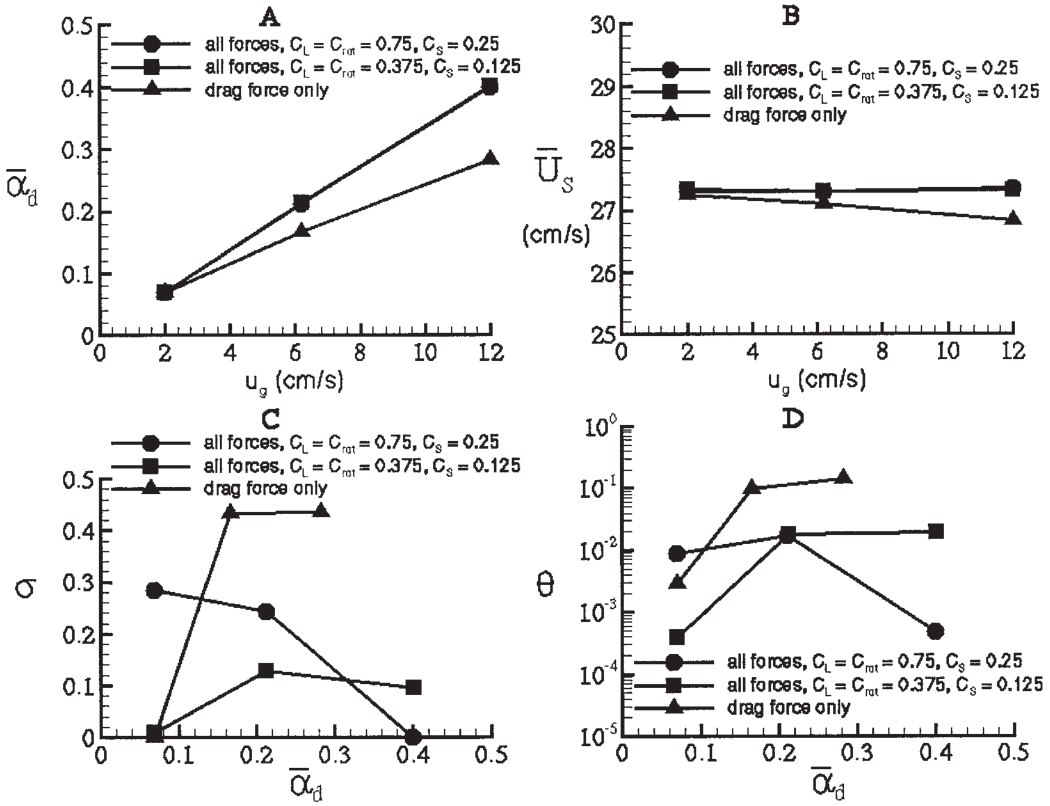

Figure 7. Quantitative analysis for transitional-flow study in 6-cm columns with the BIT model.

(A) Volume-averaged holdup; (B) volume-averaged slip velocity; (C) holdup fluctuations; (D) slip-velocity fluctuations.

should yield a transitional-flow profile, and an inlet air velocity of 12 cm/s should yield slug flow. When only the drag force is enabled, an inlet air velocity of 2 cm/s (Figure 8A) yields the expected homogeneous-flow profile. Increasing the inlet velocity to 6.2 cm/s (Figure 8B) results in a nonuniform profile with a high volume fraction of water along the column walls and small plumes of air in the center of the column. The profile for an inlet flow of 6.2 cm/s (Figure 8B) could be considered transitional because it shows a higher degree of inhomogeneous behavior than that of the profile for an inlet flow of 2 cm/s (Figure 8A), but a lower degree of inhomogeneous behavior than that of the profile for an inlet flow of 12 cm/s (Figure 8C). Using an inlet velocity of 12 cm/s does not yield the expected slug-flow profile, but instead results in a profile with a pronounced bubble plume at the bottom of the column. This plume travels upward before breaking into smaller, air-rich structures in the middle of the column. In contrast, regions of high water volume fraction are confined to the walls. With only drag enabled, the predicted instantaneous flow field thus has a "core-annular" structure that one would normally associate with much higher gas flow rates. Moreover, the transition from homogeneous to core-annular flow is very abrupt (see Figure 7C), unlike the large transitional range expected from Figure 1. We thus conclude that the use of the BIT and drag-force model alone cannot adequately represent flow-regime transitions in bubble columns.

When all forces are enabled with $C_L = C_{rot} = 0.375$ and $C_S = 0.125$, an inlet air velocity of 2 cm/s (Figure 9A) yields the expected homogeneous-flow profile. Using an inlet flow of 6.2 cm/s (Figure 9B) yields a transitional-flow profile, which appears homogeneous in the bottom half of the column and reveals faint, horizontally banded structures in the top half of the column. The bands can also be considered as rising plane waves, indicating a transition from homogeneous flow to inhomogeneous behavior. It may be noted that Olmos et al.[54] reported radially uniform gas holdup profiles for low superficial gas velocities characteristic of homogeneous flow. These profiles appeared parabolic as gas velocity increased, indicative of either transitional or heterogeneous flow. Additionally, Michele and Hempel[31] observed that a superficial gas velocity of 6 cm/s indicated the start of the heterogeneous-flow regime. Increasing the inlet air velocity to 12 cm/s (Figure 9C) results in a flow profile with more pronounced banded structures that originate as horizontal bands near the bottom of the column. As these bands progress upward, they become parabolic in appearance and seem to represent bubble swarms that extend across the column diameter. The bands maintain nearly the same width, except at the top of the column, where outflow effects become significant. In our opinion, this is the closest qualitative representation of slug flow that can be achieved when neglecting bubble coalescence. Such a profile would be expected for a 6-cm column with an inlet air velocity of 12 cm/s.

Figure 9D illustrates the flow profile for the 6-cm column with an inlet air velocity of 12 cm/s, but with periodic boundary conditions for the column walls. This flow profile also has pronounced banded structures originating as horizontal bands near the bottom of the column. However, these structures remain horizontal as they progress upward. Unlike the para-

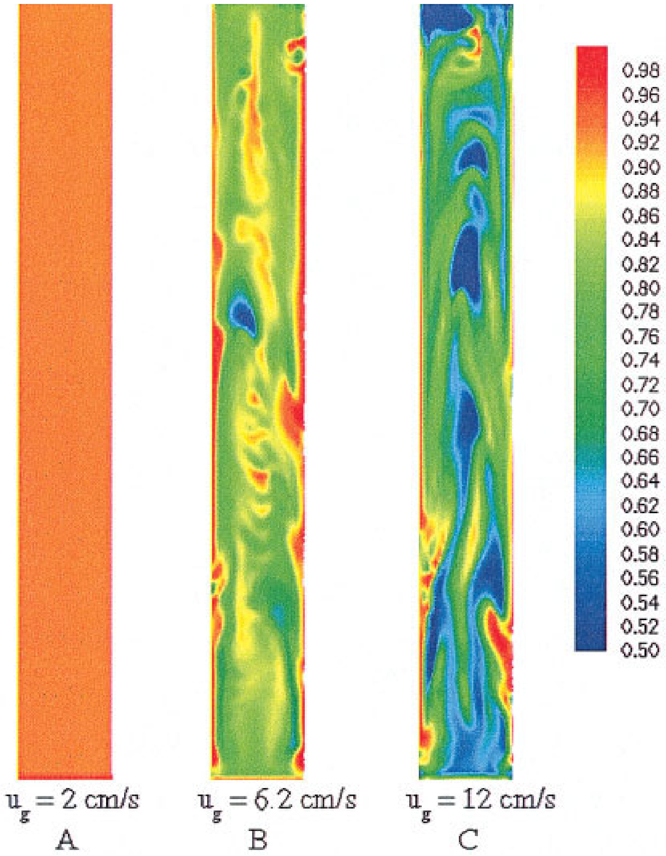

Figure 8. Water volume-fraction profiles for transitional-flow study.

Only drag force is enabled with $C_{vm} = C_L = C_{rot} = C_S = 0.0$.

bolic bands observed when free-slip boundary conditions are used (Figure 9C), the bands have different widths when periodic boundary conditions are used (Figure 9D). For both cases, these bands rise on average with a velocity of about 1 cm/s (compared to a bubble rise velocity near 27 cm/s). Studying how the centerline values of α_d vary with column height revealed that the width of the bands is about 2 cm. Extracting data for both α_d and $u_{d,y}$ at a fixed height of 40 cm and determining how both quantities oscillate with time produced wavelengths corresponding to a frequency of nearly 2 s. Dividing the average bandwidth (2 cm) by the average frequency (2 s) results in an average band rise velocity of 1 cm/s.

Note that the blue bands in Figures 9C and 9D have bubble volume fractions near 50%. If bubble coalescence were included in the model, it can be expected that coalescence rates would be relatively large at such high volume fractions, and thus that slugs (similar to those shown in Figure 2) would form in these regions. Therefore, we can conclude that the combination of the BIT model and all force models with $C_L = C_{rot} = 0.375$ and $C_S = 0.125$ yields a reasonable representation of transitional-flow behavior in small (6-cm) columns.

Effect of bubble size on flow structures

The banded flow structures observed in Figures 9C and 9D resulted from simulations in which the bubble diameter was set to 4 mm (Re $\approx$ 1093). As discussed earlier, varying the bubble Re plays an important role in the stability of the simulations using a 2 cm/s inlet air velocity. Thus, we want to determine the effect of bubble Re on the flow structures resulting from high-flow-rate (12 cm/s) simulations. Because the use of the BIT model and all force models with $C_L = C_{rot} = 0.375$ and $C_S = 0.125$ results in acceptable representations of homogeneous and transitional flow, only this combination of parameters is applied toward this study. The liquid inlet velocity is held constant at 1.6 cm/s, and both boundary-condition cases (free-slip and periodic) are considered. The value for the bubble diameter is varied from 0.5 to 4 mm, corresponding to Re ranging from about 25 to 1100. Simulation conditions are summarized in Table 2.

Figure 10 presents the quantitative analysis for high-flow-rate simulations in 6-cm columns. The values for volume-averaged gas holdup ($\bar{\alpha}_d$), volume-averaged slip velocity ($\bar{U}_S$), holdup fluctuations (σ), and slip-velocity fluctuations (θ) were computed as discussed previously. Both $\bar{\alpha}_d$ and $\bar{U}_S$ are plotted as functions of bubble diameter (d_b), and σ and θ are plotted as functions of Re. Overall, changing the boundary conditions from free-slip to periodic does not result in large differences in the quantitative analysis. On the other hand, volume-averaged holdup decreases with increasing d_b, whereas the volume-averaged slip velocity increases with increasing d_b in nearly the same way as seen previously for the homogeneous-flow predictions (Figures 5B and 6B). These results further confirm that the volume-averaged quantities are determined solely by the drag coefficient, which in turn depends on Re by input bubble diameter. Thus, even for high-flow-rate simulations, comparisons of the average holdup and average slip velocity with experimental data will not greatly aid in validating the predictive capabilities of the two-fluid model.

The dependency of stability on bubble Re for the high-flow-rate simulations is illustrated in the plots for σ and θ (Figures 10C and 10D). As Re increases, the values for σ and θ decrease until Re is $\cong$500, after which both σ and θ increase with increasing bubble Re. A similar trend was observed for the homogeneous-flow simulations (see Figure 6); however, for the homogeneous-flow predictions, σ and θ reached minimum values when Re $\approx$ 210 (Figures 6C and 6D). Additionally, the maximum values of σ and θ computed are on the order of 0.1, higher overall than those computed from the homogeneous-flow predictions that used the same parameter values (BIT, all forces enabled with $C_L = C_{rot} = 0.375$ and $C_S = 0.125$). This tendency away from stability is expected because an increase in the gas flow rate typically results in unstable flow.[2] However, when $200 < \text{Re} < 500$ ($d_b \approx$ 1.5–2.5 mm), the values of σ and θ indicate a degree of stability closer to that observed for the homogeneous flow. To our knowledge, there are no experimental data for varying bubble size, and in turn bubble Re, that can be used to validate the transition from homogeneous to unstable flow shown in Figure 10. However, given the sensitivity of the model predictions to the bubble diameter, such experiments would be extremely useful for testing the force models.

Figure 11 illustrates the effect of bubble Re on the banded flow structures, such as those presented in Figures 9C and 9D. In this figure, the centerline values of the instantaneous gas holdup (α_d) are plotted as a function of column height. When Re is about 26, corresponding to the smallest bubble size studied, the centerline values of α_d vary randomly as column height increases. These fluctuations correspond to random vor-

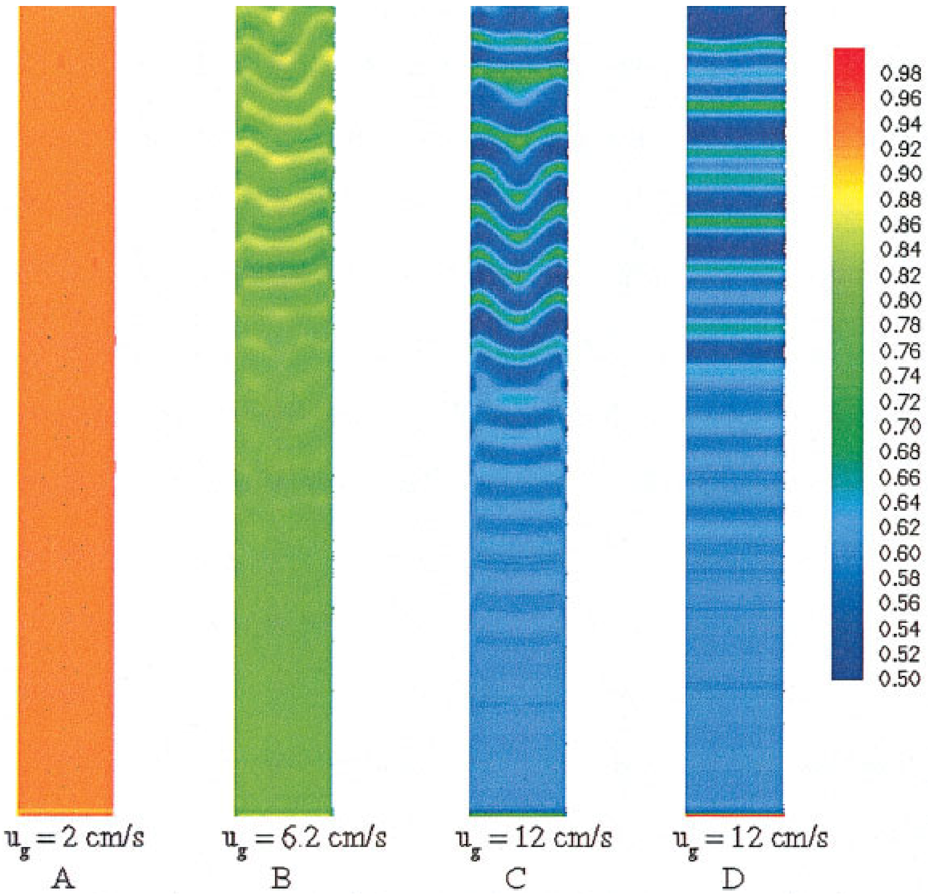

Figure 9. Water volume-fraction profiles for transitional-flow study.

All forces are enabled with $C_{vm} = 0.5$, $C_L = C_{rot} = 0.375$, and $C_S = 0.125$. (A)–(C) correspond to simulations with free-slip boundary conditions, whereas (D) corresponds to a simulation with periodic boundary conditions.

tical structures in the velocity fields that are similar to low-Reynolds-number turbulence observed in single-phase flows. Note that the average gas holdup for such small bubbles is extremely high (80%) for this gas flow rate. Because the holdup corresponding to close-packed spheres is about 64%, it is unlikely that such a high holdup could be observed experimentally.

In Figure 11, the centerline holdup profiles for medium-sized bubbles (Re $\approx$ 210 and 504) are flat, corresponding to the smaller computed values of σ and θ (Figures 10C and 10D) for these bubble Re and the absence of banded flow structures. Increasing Re to about 880 produces oscillations in α_d along the column centerline after a column height of nearly 10 cm. These oscillations correspond to banded structures and have a wavelength of about 2 cm. Their amplitude increases with increasing column height until a height of about 30 cm, after which the amplitude remains constant. This behavior corresponds to the sudden increase in the values of σ and θ (Figures 10C and 10D). As seen in Figures 9C and 9D, the periodicity of the banded structures is enhanced by the use of free-slip (as opposed to periodic) boundary conditions.

In Figure 11, further increasing Re to approximately 1093, corresponding to the largest bubble size studied, again produces oscillations that originate after a column height of approximately 10 cm and have a wavelength of about 2 cm. However, these oscillations have a higher amplitude and are less ordered than those resulting from Re $\approx$ 880. Such behavior corresponds to the highest values of σ and θ presented in Figures 10C and 10D. It is therefore concluded that the bubble Reynolds number plays a significant role in the stability of high-flow-rate simulations and the appearance of flow structures. The bands, presumed to be indicative of slug flow as expected for a 6-cm column with an air inlet flow rate of 12 cm/s, occur only for bubbles for which the Reynolds number is $\gtrsim$500. We expect that a linear stability analysis[84,85] for these cases may provide further insight toward the effect of bubble Reynolds number on the stability of high-flow-rate simulations.

Effect of liquid coflow

The previously discussed high-flow-rate simulations (such as Figure 11) used a constant inlet liquid velocity of 1.6 cm/s, one of the experimental inlet values, used in small-diameter columns, performed by Garnier et al.[56,57] These experiments studied the effect of liquid coflow by considering four different values of the superficial liquid velocity u_l. They observed that for high values of dispersed-phase holdup, large-scale, downward motions would occur at the column outlet for u_l = 1.6 cm/s. Such instabilities were not observed experimentally for larger values of u_l. To study the effect of liquid coflow on flow

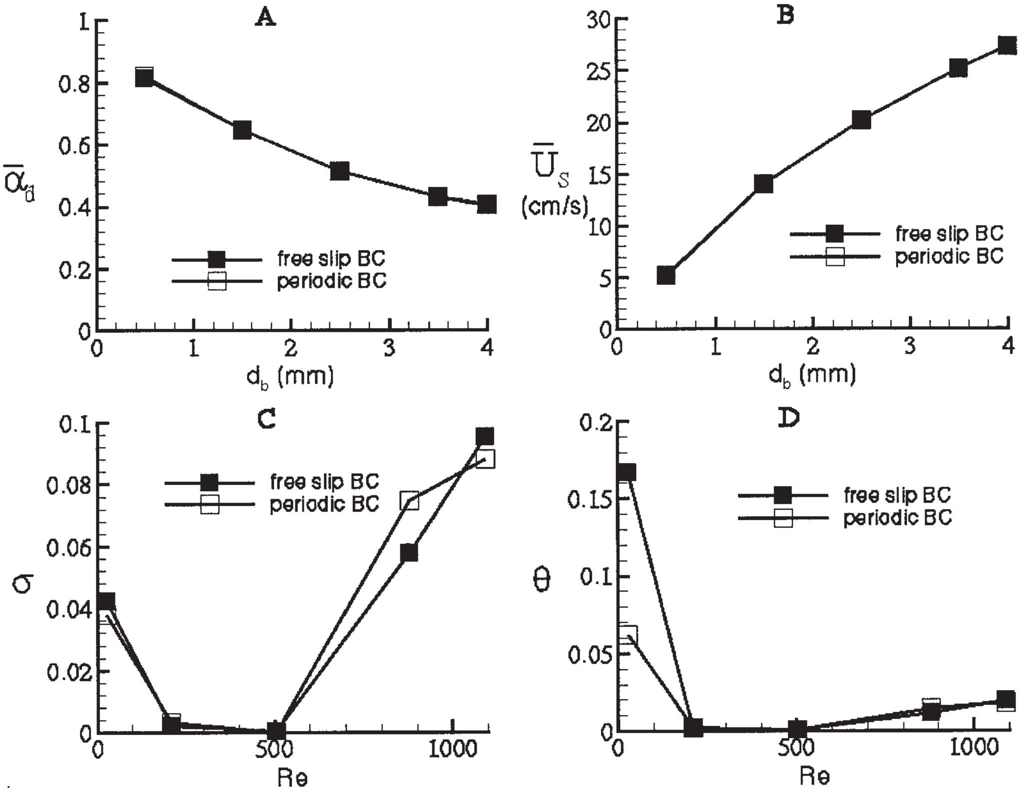

Figure 10. Quantitative analysis for high-flow-rate (12 cm/s) study in 6-cm columns with the BIT model.

All forces are enabled with $C_{vm} = 0.5$, $C_L = C_{rot} = 0.375$, and $C_S = 0.125$. (A) volume-averaged holdup; (B) volume-averaged slip velocity; (C) holdup fluctuations; (D) slip-velocity fluctuations.

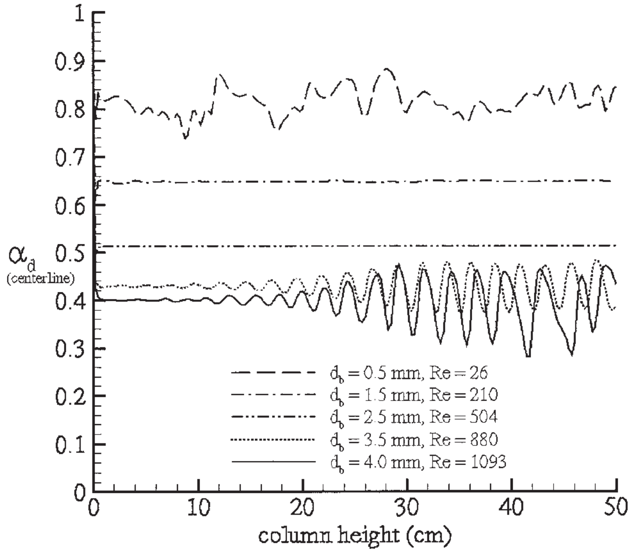

Figure 11. Effect of bubble diameter on the stability and appearance of flow structures observed for high-flow-rate (12 cm/s) simulations using free-slip boundary conditions.

All forces are enabled with $C_{vm} = 0.5$, $C_L = C_{rot} = 0.375$, and $C_S = 0.125$.

stability, 2-D simulations are carried out for three inlet liquid velocities: 0, 1.6, and 3.3 cm/s. In these simulations, the bubble diameter is set to 4 mm (Re ≈ 1093), and the inlet air velocity is held constant at 12 cm/s. The BIT model and all force models with $C_L = C_{rot} = 0.375$ and $C_S = 0.125$ are applied in this study. Note that as liquid coflow is increased, average gas holdup will slightly decrease.

Figure 12 presents the centerline values of the holdup (α_d) as a function of column height for each value of u_l to demonstrate the effect of liquid coflow on the banded flow structures. When no coflow is applied, oscillations in α_d originate at a column height of 4 cm, and are not consistent in either wavelength or amplitude as column height increases. Increasing u_l to 1.6 cm/s results in oscillations in α_d that originate at a column height of nearly 10 cm. The wavelength of the banded structures is about 2 cm, and the amplitude increases with column height up to a height of about 30 cm, after which the amplitude is nearly constant. At a height of about 40 cm, however, both the wavelength and amplitude of the oscillations vary again, reflecting instability at the column outlet. Further increasing u_l to 3.3 cm/s produces oscillations that originate at a column height of about 12 cm. These oscillations maintain a wavelength of about 2 cm, whereas the amplitude increases with column height up to a height of 40 cm, after which the amplitude is nearly constant. Average band rise velocity was determined again by dividing the average bandwidth by the average frequency, and for all three cases the bands rise on average with a velocity of about 1 cm/s, thus showing no significant depen-

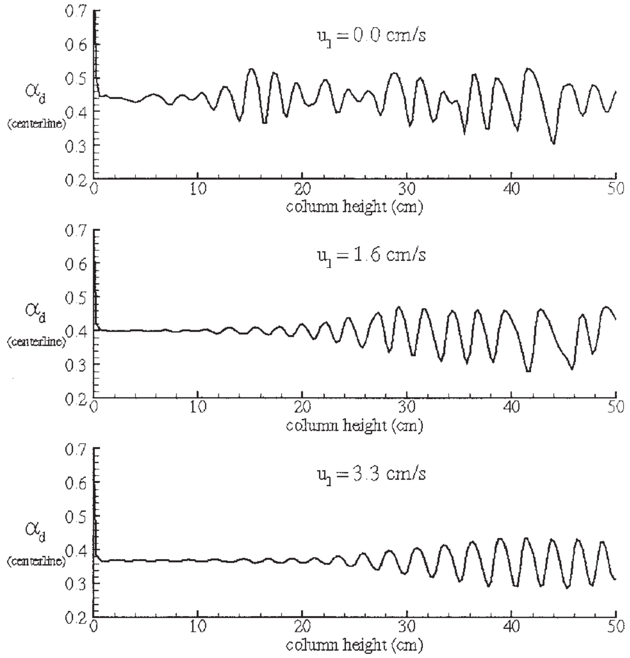

Figure 12. Effect of liquid coflow on the stability and appearance of flow structures observed for high-flow-rate (12 cm/s) simulations.

All forces are enabled with $C_{vm} = 0.5$, $C_L = C_{rot} = 0.375$, and $C_S = 0.125$. The bubble Reynolds number Re is approximately equal to 1093 for this case.

dency on liquid coflow. However, the behavior of the oscillations of the centerline values of α_d with respect to variations in liquid coflow further confirms that an increase in u_l results in enhanced stability of the high-gas-flow-rate simulations.

Effect of column diameter

Our final goal is to determine whether the combined use of the BIT model and all force models with $C_L = C_{rot} = 0.375$ and $C_S = 0.125$ will predict the correct behavior for larger-diameter columns (see Figure 1). Scale-up is an important aspect in the design of a bubble column. Krishna et al.[49] showed the limitations in the applicability of the empirical correlations over a range of column diameters. As the column diameter is increased, the length scales of the flow eddies also increase, resulting in enhanced turbulence in the churn-turbulent regime. Turbulence models for multiphase flows should scale accordingly. On the other hand, in the homogeneous regime the flow remains stable for all column diameters (see Figure 1). Thus, the applicability of two-fluid CFD models to larger-diameter columns must be tested. First, simulations for 20- and 40-cm columns, using an inlet air velocity of 2 cm/s and an inlet water velocity of 0 cm/s, are reported. As discussed previously, three force-model combinations are used: (1) all forces enabled, with $C_{vm} = 0.5$, $C_L = C_{rot} = 0.75$, and $C_S = 0.25$; (2) all forces enabled, with $C_{vm} = 0.5$, $C_L = C_{rot} = 0.375$, and $C_S = 0.125$; and (3) only drag force enabled, with $C_{vm} = C_L = C_{rot} = C_S = 0$. Quantitative analysis is performed as described in earlier sections. The values for volume-averaged gas holdup ($\bar{\alpha}_d$) and volume-averaged slip velocity ($\bar{U}_S$) are plotted as functions of bubble diameter (d_b), and the holdup fluctuations (σ) and slip-velocity fluctuations (θ) are plotted as functions of bubble Re. Conditions for these simulations are summarized in Table 2. Figure 13 presents the quantitative analysis for this scale-up study.

According to the flow-regime map (Figure 1), columns of 6, 20, or 40 cm in diameter using an inlet air velocity of 2 cm/s should all operate in the homogeneous-flow regime. It may be noted that the experiments of Chen et al.,[86] performed on columns of 20, 40, and 80 cm in diameter, showed that the power spectrum was not affected by varying the column diameter. However, Kolmogorov entropy decreased with increasing column diameter, and uniform radial holdup profiles were observed in only the widest column.[86] Ruzicka et al.[87] carried out experiments on 14-, 29-, and 40-cm columns, and reported that an increase in column size decreased homogeneous flow stability and enhanced flow regime transitions. However, Forret et al.[88] performed experiments on columns of 15, 40, and 100 cm in diameter and found that average holdup was independent of column diameter, whereas liquid velocity and the axial dispersion coefficient increased with column diameter. Our work, presented in Figure 13, shows that regardless of column diameter, forces enabled, or parameter values, the volume-averaged quantities calculated for each bubble diameter are nearly the same. Thus, as discussed previously, experimental and computational data for average holdup and slip velocity are useful for parameterizing the drag coefficient, but not for validating the scale-up of two-fluid CFD models.

Because enabling all forces with $C_L = C_{rot} = 0.375$ and $C_S = 0.125$ results in homogeneous flow profiles for 6-cm columns, only this force model combination is shown in the curves for σ and θ (Figures 13C and 13D). Values of σ and θ decrease with increasing bubble Reynolds number until Re is nearly equal to 210, after which both σ and θ increase slightly with increasing bubble Re. Additionally, as Re decreases both σ and θ approach a constant value between 10^{-1} and 10^{-2}. Such behavior was also observed in Figure 6 for the 6-cm column. There does not appear to be a significant difference among column diameters for σ and θ in Figure 13 (that is, with the BIT model, $C_L = C_{rot} = 0.375$, and $C_S = 0.125$). Overall, we can conclude that the two-fluid model with the BIT model and all force models with $C_L = C_{rot} = 0.375$ and $C_S = 0.125$ correctly predicts homogeneous flow for all values of the column diameter. We note, however, that it would be very difficult to introduce bubbles uniformly in a large-diameter column, which inevitably would yield inhomogeneous flow.[58]

Figure 14 shows a qualitative comparison between a 6- and a 40-cm column, both using an inlet air velocity of 12 cm/s and an inlet water velocity of 1.6 cm/s. For these simulations, the bubble diameter is set to 4 mm (Re $\approx$ 1093), coalescence is neglected, the BIT model is included, and all forces are enabled with $C_L = C_{rot} = 0.375$ and $C_S = 0.125$. Simulation conditions are summarized in Table 2. According to the flow-regime map (Figure 1), a 6-cm column with an inlet air velocity of 12 cm/s should exhibit slug flow, whereas a 40-cm column with the same inlet flow rate should exhibit churn-turbulent flow. The 6-cm column, as seen previously in Figure 9C, shows horizontal banded structures that are originally flat near the bottom of the column, and become parabolic in appearance as they travel upward. Because these bands appeared to represent bubble swarms of the width of the column diameter, it was previously concluded that the 6-cm column would exhibit slug flow (as

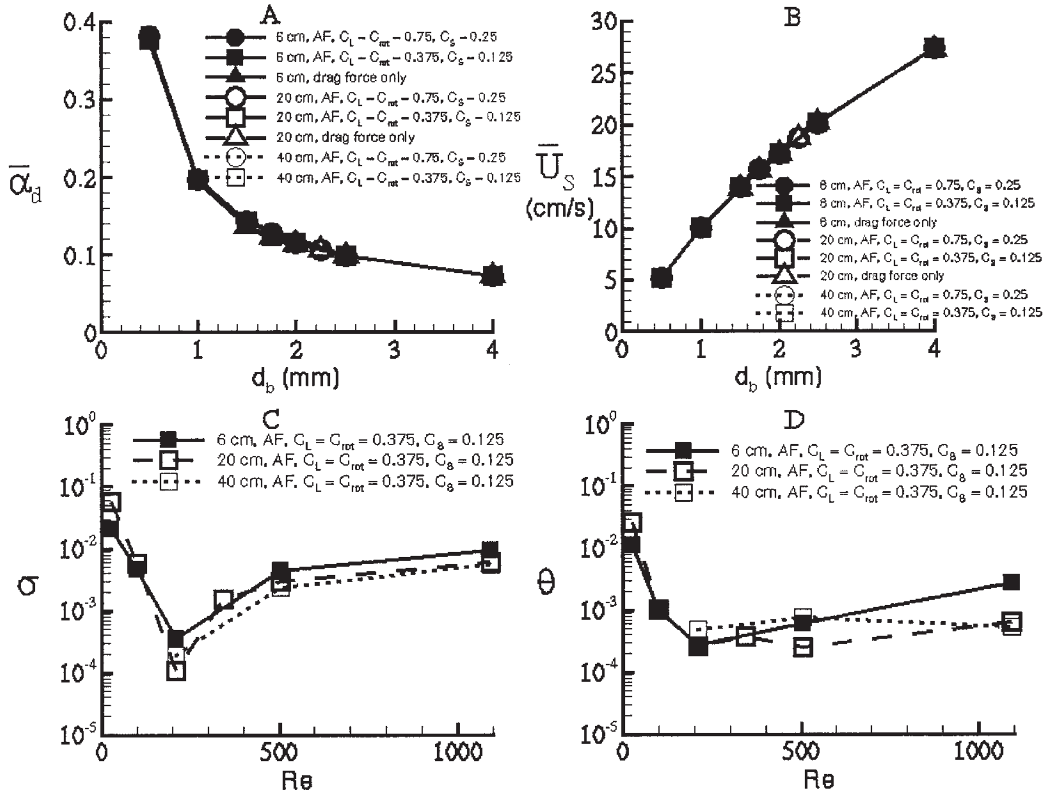

Figure 13. Quantitative analysis of the effect of column diameter in the homogeneous-flow regime.

(A) Volume-averaged holdup; (B) volume-averaged slip velocity; (C) holdup fluctuations; (D) slip-velocity fluctuations.

predicted by the flow-regime map in Figure 1) if bubble coalescence were included in the model. The simulation for the 40-cm column does not yield churn-turbulent flow as predicted by the flow-regime map. Instead, as seen in the 6-cm column, horizontal bands form and persist throughout the column, becoming increasingly pronounced as they reached the top of the column. As in the 6-cm column, the bubble volume fraction in these bands is near 50%, and thus relatively large coalescence rates would be expected. Moreover, given that the thickness of the bands in the 40-cm column is approximately the same as that of bands in the 6-cm column, it can be expected that the average bubble sizes generated by coalescence in the two columns will be nearly the same. Thus, in the 40-cm column, the average bubble size would be much smaller than the column diameter. Therefore, because such bubbles would not span the entire column, it may indeed be possible to generate churn-turbulent flow in the 40-cm column if a bubble coalescence model, such as that described by Sanyal et al.,[89] were included in the two-fluid model.

Conclusions

As clearly demonstrated in this work, the ability of widely used multiphase CFD models to predict flow regimes in bubble columns depends significantly on grid resolution and model formulation. It is determined that sufficient resolution is achieved when a grid spacing of 0.25 cm or smaller is used for air–water bubble columns. In contrast, previous CFD studies reported in the literature used grids of ≥0.5 cm, and thus their results are contaminated by numerical diffusion. The importance of grid resolution has also recently been reported by Sokolichin et al.[7] and Chen and Fan.[8] Unlike earlier investigations that used inadequate grid resolution, it is found here that flow predictions are highly dependent on the model formulation. The bubble Reynolds number, the effective viscosity model, and the force models (that is, drag, virtual mass, lift, rotation, and strain) and parameter values work together to play a significant role in the flow profiles observed in grid-independent CFD simulations of bubble columns.

For low air flow rates (such as 2 cm/s), homogeneous flow is predicted in 6-cm columns when Sato's BIT model is included, and all force models are enabled with $C_L = C_{rot} = 0.375$ and $C_S = 0.125$. When applying these settings for 20- and 40-cm columns operating with 2 cm/s inlet air velocity, the expected tendency toward homogeneous flow is observed. Therefore, the two-fluid model with these modifications can be used successfully for column scale-up in the homogeneous flow regime. Additionally, using the BIT model and all force models with $C_L = C_{rot} = 0.375$ and $C_S = 0.125$ also appears to yield an adequate representation of the transition from homogeneous flow for 6-cm columns. For high gas flow rates (such as 12 cm/s), we have shown that the bubble Reynolds number has a significant effect on the flow structures observed in simulations of 6-cm columns. Small bubbles ($d_b = 0.5$ mm or Re $\approx$ 25) result in random structures, whereas large bubbles ($d_b = 3.5$–4.0 mm or Re $\approx$ 880–1100) produce ordered horizontal bands or swarms. Additionally, we demonstrate that increasing the liquid coflow enhances the stability of the high-air-flow-rate simulations, as well as the resulting flow structures. Applying

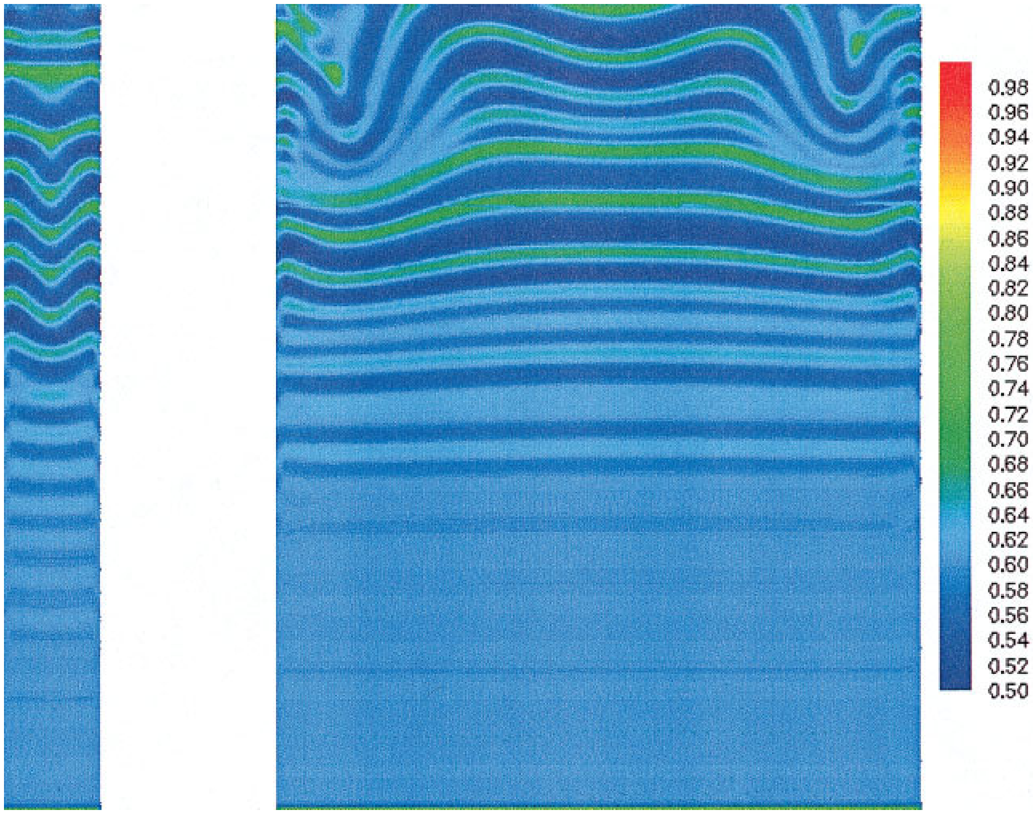

Figure 14. Qualitative analysis of the effect of column diameter on the water volume-fraction profiles in the heterogeneous-flow regime.

Left: 6-cm column. Right: 40-cm column.

the BIT model and all force models with $C_L = C_{rot} = 0.375$ and $C_S = 0.125$ does not result in churn-turbulent flow with column scale-up for high-flow-rate simulations, most likely resulting from the absence of a bubble-coalescence model. Experimental testing of the high-flow-rate simulations discussed in this work would likely benefit the modeling community by allowing them to determine whether existing closures are missing important physics needed to describe high gas flow rates in the absence of coalescence.

Having successfully demonstrated that the two-fluid model can predict flow transitions in bubble columns, in future work we plan to investigate its ability to predict the flow patterns observed by Harteveld et al.[58] for nonuniform gas-phase inlet boundary conditions. Finally, we plan to perform a linear stability analysis for both the 2-D and 3-D flow predictions. Jackson[84] performed such an analysis for fluidized beds to examine how small perturbations will affect the stability of the uniformly fluidized state. He determined the dispersion relations that describe the growth or decay rates for small-amplitude disturbance waves. We plan to follow his procedure and derive the dispersion relations corresponding to the two-fluid model present in CFDLib.

Acknowledgments

We are grateful to the National Science Foundation (Grant CTS-0112571) for funding this work. Additionally, the authors thank Dr. Kashiwa at Los Alamos National Laboratory for his assistance with CFDLib, and Dr. Toseland at Air Products and Chemicals for his input and interest in this project.

Notation

Ca_γ = capillary number[67]
C_{att} = attraction coefficient (Appendix A)
C_{BP} = virtual-mass coefficient of an isolated bubble
C_{BT} = proportionality constant for bubble-induced turbulence model
C_D = drag coefficient
C_L = lift coefficient
C_{rep} = repulsion coefficient (Appendix A)
C_{rot} = rotation coefficient
C_S = strain coefficient
C_{vm} = virtual-mass coefficient
d_b = bubble diameter, mm
Eo = Eötvös number, dimensionless
$\boldsymbol{F}_{att}$ = attraction force (Appendix A)
$\boldsymbol{F}_D$ = drag force
$\boldsymbol{F}_{fk}$ = sum of interaction forces
$\boldsymbol{F}_L$ = lift force
$\boldsymbol{F}_{rep}$ = repulsion force (Appendix A)
$\boldsymbol{F}_{rot}$ = rotation force
$\boldsymbol{F}_S$ = strain force
$\boldsymbol{F}_{vm}$ = virtual-mass force
$\boldsymbol{G}$ = sum of symmetric and antisymmetric tensors used to calculate $\boldsymbol{F}_{att}$ and $\boldsymbol{F}_{rep}$ (Appendix A)
$\boldsymbol{g}$ = gravitational force
$\boldsymbol{I}$ = Kelvin impulse, N/s (Table 1[21-23])
P_k = bubble pressure model applied to phase k
p = pressure

r_b = bubble radius, mm
Re = bubble Reynolds number, dimensionless
$\boldsymbol{S}_k$ = phase strain rate tensor (Appendix A)
$\boldsymbol{u}_g$ = inlet gas velocity, cm/s
$\boldsymbol{u}_k$ = velocity of phase k, cm/s
$\boldsymbol{u}_l$ = inlet water velocity, cm/s
$\boldsymbol{u}_v$ = phase-averaged velocity, cm/s
$\boldsymbol{U}_S$ = slip velocity, cm/s (designation for the present work)
$\boldsymbol{U}_T$ = terminal bubble velocity or bubble rise velocity, m/s (Table 1[36,49])
V_b = bubble volume, m^3 (Table 1[21-23])

Greek letters

α_k = volume fraction of phase k, dimensionless
α_dcp = gas void fraction at close packing, dimensionless
$\mu_{\mathrm{o},k}$ = molecular viscosity of phase k
$\mu_{\mathrm{eff},k}$ = effective viscosity of phase k
$\mu_{\mathrm{t},k}$ = turbulent viscosity for phase k
ν_c = kinematic molecular viscosity for continuous phase
ν_t = kinematic turbulent viscosity
θ = slip velocity fluctuations
ρ_k = density of phase k
ρ_v = volumetric density
σ = gas holdup fluctuations
τ = surface tension, N/m

Subscripts

c = continuous phase
d = dispersed phase
f = index for sum of interfacial forces
k = general phase

Literature Cited

1. Vitankar VS, Dhotre MT, Joshi JB. A low Reynolds number k–ε model for the prediction of flow pattern and pressure drop in bubble column reactors. *Chem Eng Sci*. 2002;57:3235-3250.
2. Shah YT, Deckwer W-D. Hydrodynamics of bubble columns. In: Cheremisinoff NP, Gupta R, eds. *Handbook of Fluids in Motion*. Ann Arbor, MI: Ann Arbor Science; 1983:583-620.
3. Joshi JB. Computational flow modelling and design of bubble column reactors. *Chem Eng Sci*. 2001;56:5893-5933.
4. Jakobsen HA, Sannaes BH, Grevskott S, Svendsen HF. Modelling of vertical bubble-driven flows. *Ind Eng Chem Res*. 1997;36:4052-4074.
5. Joshi JB, Vitankar VS, Kulkarni AA, Dhotre MT, Ekambara K. Coherent flow structures in bubble column reactors. *Chem Eng Sci*. 2002;57:3157-3183.
6. Laín S, Bröder D, Sommerfeld M, Göz MF. Modelling hydrodynamics and turbulence in a bubble column using the Euler–Lagrange procedure. *Int J Multiphase Flow*. 2002;28:1381-1407.
7. Sokolichin A, Eigenberger G, Lapin A. Simulation of buoyancy driven bubbly flow: Established simplifications and open questions. *AIChE J*. 2004;50:24-45.
8. Chen C, Fan LS. Discrete simulation of gas–liquid bubble columns and gas–liquid–solid fluidized beds. *AIChE J*. 2004;50:288-301.
9. Rice RG, Geary NW. Prediction of liquid circulation in viscous bubble columns. *AIChE J*. 1990;36:1339-1348.
10. Geary NW, Rice RG. Circulation and scale-up in bubble columns. *AIChE J*. 1992;38:76-82.
11. Burns LF, Rice RG. Circulation in bubble columns. *AIChE J*. 1997; 43:1390-1402.
12. Vitankar VS, Joshi JB. A comprehensive one-dimensional model for prediction of flow pattern in bubble columns. *Chem Eng Res Des*. 2002;80:499-512.
13. Sokolichin A, Eigenberber G. Gas–liquid flow in bubble columns and loop reactors: Part I. Detailed modeling and numerical simulation. *Chem Eng Sci*. 1994;49:5735-5746.
14. Sokolichin A, Eigenberger G, Lapin A, Lübbert A. Dynamical numerical simulation of gas–liquid two-phase flows. Euler/Euler versus Euler/Lagrange. *Chem Eng Sci*. 1997;52:611-626.
15. Sanyal J, Vásquez S, Roy S, Dudukovic MP. Numerical simulation of gas–liquid dynamics in cylindrical bubble column reactors. *Chem Eng Sci*. 1999;54:5071-5083.
16. Buscaglia GC, Bombardelli FA, García MH. Numerical modeling of large-scale bubble plumes accounting for mass transfer effects. *Int J Multiphase Flow*. 2002;28:1763-1785.
17. Rigopoulos S, Jones A. A hybrid CFD–reaction engineering framework for multiphase reactor modeling: Basic concept and application to bubble column reactors. *Chem Eng Sci*. 2003;58:3077-3089.
18. Torvik R, Svendsen HF. Modelling of slurry reactors. A fundamental approach. *Chem Eng Sci*. 1990;45:2325-2332.
19. Lapin A, Lübbert A. Numerical simulation of the dynamics of two-phase gas–liquid flows in bubble columns. *Chem Eng Sci*. 1994;49: 3661-3674.
20. Grevskott S, Sannaes BH, Dudukovic MP, Hjarbo KW, Svendsen HF. Liquid circulation, bubble size distributions, and solids movement in two- and three-phase bubble columns. *Chem Eng Sci*. 1996;51:1703-1713.
21. Delnoij E, Kuipers JAM, van Swaaij WPM. Computational fluid dynamics applied to gas–liquid contactors. *Chem Eng Sci*. 1997;52: 3623-3638.
22. Delnoij E, Lammers FA, Kuipers JAM, van Swaaij WPM. Dynamic simulation of dispersed gas–liquid two-phase flow using a discrete bubble model. *Chem Eng Sci*. 1997;52:1429-1458.
23. Delnoij E, Kuipers JAM, van Swaaij WPM. Dynamic simulation of gas–liquid two-phase flow: Effect of column aspect ratio on the flow structure. *Chem Eng Sci*. 1997;52:3759-3772.
24. Sokolichin A, Eigenberger G. Applicability of the standard k–ε turbulence model to the dynamic simulation of bubble columns: Part I. Detailed numerical simulations. *Chem Eng Sci*. 1999;54:2273-2284.
25. Mudde RF, Simonin O. Two- and three-dimensional simulations of a bubble plume using a two-fluid model. *Chem Eng Sci*. 1999;54:5061-5069.
26. Pan Y, Dudukovic MP, Chang M. Dynamic simulation of bubbly flow in bubble columns. *Chem Eng Sci*. 1999;54:2481-2489.
27. Pan Y, Dudukovic MP, Chang M. Numerical investigation of gas-driven flow in 2-D bubble columns. *AIChE J*. 2000;46:434-449.
28. Pfleger D, Becker S. Modelling and simulation of the dynamic flow behaviour in a bubble column. *Chem Eng Sci*. 2001;56:1737-1747.
29. Buwa VV, Ranade VV. Dynamics of gas–liquid flow in a rectangular bubble column: Experiments and single/multi-group CFD simulations. *Chem Eng Sci*. 2002;57:4715-4736.
30. Lehr F, Millies M, Mewes D. Bubble-size distributions and flow fields in bubble columns. *AIChE J*. 2002;48:2426-2443.
31. Michele V, Hempel DC. Liquid flow and phase holdup—Measurement and CFD modeling for two- and three-phase bubble columns. *Chem Eng Sci*. 2002;57:1899-1908.
32. Zhou LX, Yang M, Lian CY, Fan LS, Lee DJ. On the second order moment turbulence model for simulating a bubble column. *Chem Eng Sci*. 2002;57:3269-3281.
33. Oey RS, Mudde RF, van den Akker HEA. Sensitivity study on interfacial closure laws in two-fluid bubbly flow simulations. *AIChE J*. 2003;49:1621-1636.
34. Olmos E, Gentric C, Midoux N. Numerical description of flow regime transitions in bubble column reactors by a multiple gas phase model. *Chem Eng Sci*. 2003;58:2113-2121.
35. Deen NG, Solberg T, Hjertager BH. Large eddy simulation of the gas–liquid flow in a square cross-sectioned bubble column. *Chem Eng Sci*. 2001;56:6341-6349.
36. Bove S, Solberg T, Hjertager BH. Numerical aspects of bubble column simulations. *Int J Chem React Eng*. 2004;2:A1.
37. Monahan S, Fox RO. Effect of grid resolution and force models. Proc of 8th Int Conf on Multiphase Flow in Industrial Plants. Alba, Italy, Sep. 18–20; 2002:69-85.
38. Sundaresan S. Modeling the hydrodynamics of multiphase flow reactors: Current status and challenges. *AIChE J*. 2000;46:1102-1105.
39. Krishna R, van Baten JM. Eulerian simulations of bubble columns operating at elevated pressures in the churn turbulent flow regime. *Chem Eng Sci*. 2001;56:6249-6258.
40. Jakobsen HA. Phase distribution phenomena in two-phase bubble column reactors. *Chem Eng Sci*. 2001;56:1049-1056.
41. Becker S, Sokolichin A, Eigenberger G. Gas–liquid flow in bubble columns and loop reactors: Part II. Comparison of detailed experiments and flow simulations. *Chem Eng Sci*. 1994;49:5747-5762.

42. Duineveld PG. *Bouncing and Coalescence of Two Bubbles in Water*. PhD Thesis. Enschede, The Netherlands: Twente University; 1994.
43. Sato Y, Sekoguchi K. Liquid velocity distribution in two-phase bubble flow. *Int J Multiphase Flow*. 1975;2:79-95.
44. Yuan Z, Michaelides EE. Turbulence modulation in particulate flows—A theoretical approach. *Int J Multiphase Flow*. 1992;18:779-785.
45. Kenning VM, Crowe CT. On the effect of particles on carrier phase turbulence in gas-particle flows. *Int J Multiphase Flow*. 1997;23:403-408.
46. Crowe CT, Gillandt I. Turbulence modulation of fluid-particle flows. A basic approach. Proc of the 3rd Int Conf on Multiphase Flow, Lyon, France; 1998.
47. Février P, Simonin O. Constitutive equations for fluid-particle velocity correlations in gas–solid turbulent flows. Proc of the 3rd Int Conf on Multiphase Flow, Lyon, France; 1998.
48. Delnoij E, Kuipers JAM, van Swaaij WPM. A three-dimensional CFD model for gas–liquid bubble columns. *Chem Eng Sci*. 1999;54:2217-2226.
49. Krishna R, Urseanu MI, van Baten JM, Ellenberger J. Influence of scale on the hydrodynamics of bubble columns operating in the churn-turbulent regime: Experiments vs. Eulerian simulations. *Chem Eng Sci*. 1999;54:4903-4911.
50. Pfleger D, Gomes S, Gilbert N, Wagner HG. Hydrodynamic simulations of laboratory scale bubble columns: Fundamental studies of the Eulerian–Eulerian modelling approach. *Chem Eng Sci*. 1999;54:5091-5099.
51. Padial NT, VanderHeyden WB, Rauenzahn RM, Yarbro SL. Three-dimensional simulation of a three-phase draft-tube bubble column. *Chem Eng Sci*. 2000;55:3261-3273.
52. Tomiyama A, Celata GP, Hosokawa S, Yoshida S. Terminal velocity of single bubbles in surface tension force dominant regime. *Int J Multiphase Flow*. 2002;28:1497-1519.
53. Morsi SA, Alexander AJ. An investigation of particle trajectories in two-phase flow systems. *J Fluid Mech*. 1972;55:193-208.
54. Olmos E, Gentric C, Vial Ch, Wild G, Midoux N. Numerical simulation of multiphase flow in bubble column reactors. Influence of bubble coalescence and break-up. *Chem Eng Sci*. 2001;56:6359-6365.
55. Olmos E, Gentric C, Poncin S, Midoux N. Description of flow regime transitions in bubble columns via laser Doppler anemometry signals processing. *Chem Eng Sci*. 2003;58:1731-1742.
56. Garnier C, Lance M, Marié JL. Measurement of local flow characteristics in buoyancy-driven bubbly flow at high void fraction. *Exp Therm Fluid Sci*. 2002;26:811-815.
57. Garnier C, Lance M, Marié JL, Mareuge I. Experiments on buoyancy-driven bubbly flows at low and high void fractions. Laboratoire de Mécanique des Fluides et d'Acoustique UMR CNRS 5509, Ecole Centrale de Lyon/Université Lyon I 69131 Ecully Cedex, France; 2002.
58. Harteveld WK, Mudde RF, van den Akker HEA. Dynamics of a bubble column: Influence of gas distribution on coherent structures. *Can J Chem Eng*. 2003;81:389-394.
59. Biesheuvel A, Gorissen WCM. Void fraction disturbances in a uniform bubbly fluid. *Int J Multiphase Flow*. 1990;16:211-231.
60. Drew DA, Passman SL. *Theory of Multicomponent Fluids*. New York, NY: Springer-Verlag; 1999.
61. Chen RC, Reese J, Fan LS. Flow structure in a three-dimensional bubble column and three-phase fluidized bed. *AIChE J*. 1994;40:1093-1104.
62. Kashiwa BA, Padial NT, Rauenzahn RM, VanderHeyden WB. A cell-centered ICE method for multiphase flow simulations. *Numerical Methods in Multiphase Flows*. Vol. 185. Proc of ASME Heat and Fluids Engineering Divisions (FED); 1994.
63. Kashiwa BA, Rauenzahn RM. A multimaterial formalism. *Numerical Methods in Multiphase Flows*. Vol. 185. Proc of ASME Heat and Fluids Engineering Divisions (FED); 1994.
64. Hirt CW, Amsden AA, Cook JL. An arbitrary Lagrangian–Eulerian computing method for all flow speeds. *J Comput Phys*. 1974;14:227-253.
65. Harlow FH, Amsden AA. Numerical calculation of multiphase fluid flow. *J Comput Phys*. 1975;17:19-52.
66. Spelt PDM, Sangani A. Properties and averaged equations for flows of bubbly liquids. *Appl Sci Res*. 1998;58:337-386.
67. Sankaranarayanan K, Sundaresan S. Lift force in bubbly suspensions. *Chem Eng Sci*. 2002;57:3521-3542.
68. Batchelor GK. A new theory on the instability of a uniform fluidized bed. *J Fluid Mech*. 1988;193:75-110.
69. Sato Y, Sadatomi M, Sekoguchi K. Momentum and heat transfer in two-phase bubble flow I. *Int J Multiphase Flow*. 1981;7:167-177.
70. Troshko AA, Hassan YA. Modeling of turbulent bubbly pipe flow with the CFX 4.2 computer program. http://www.iahr.org/membersonly/grazproceedings99/doc/000/000/054.htm; 1999.
71. Kashiwa BA, VanderHeyden WB. Toward a general theory for multiphase turbulence. Part I: Development and gauging of the model equations. Los Alamos Report No. LA 13773 MS; Los Alamos, NM: Los Alamos National Laboratory; 2000.
72. Clift R, Grace JR, Weber ME. *Bubbles, Drops, and Particles*. New York, NY: Academic Press; 1978.
73. Joshi JB, Parasu UV, Prasad Ch V, Phanikumar DV, Deshpande NS, Thakre SS, Thorat BN. Gas holdup structures in bubble column reactors. *PINSA*. 1998;64:441-567.
74. Sankaranarayanan K, Shan X, Kevrekidis IG, Sundaresan S. Analysis of drag and virtual mass forces in bubbly suspensions using an implicit formulation of the lattice Boltzmann method. *J Fluid Mech*. 2002;452:61-96.
75. Drew DA, Cheng L, Lahey RT. The analysis of virtual mass effects in two-phase flow. *Int J Multiphase Flow*. 1979;5:233-242.
76. Cook TL, Harlow FH. Vortices in bubbly two-phase flow. *Int J Multiphase Flow*. 1986;12:35-61.
77. Homsy GM, El-Kaissy MM, Didwania A. Instability waves and the origin of bubbles in fluidized beds—II. Comparison with theory. *Int J Multiphase Flow*. 1980;6:305-318.
78. Biesheuvel A, Spoelstra S. The added mass coefficient of a dispersion of spherical gas bubbles in liquid. *Int J Multiphase Flow*. 1989;15:911-924.
79. Hunt JCR, Auton TR, Sene K, Thomas NH, Kowe R. Proc of ICHMT Int Seminar on Transient Phenomena in Multiphase Flow, Dubrovnik, Yugoslavia; 1987:103-125.
80. Arnold GS, Drew DA, Lahey RT. Derivation of constitutive equations for interfacial force and Reynolds stress for a suspension of spheres using ensemble cell averaging. *Chem Eng Commun*. 1989;86:43-54.
81. Auton TR. The lift force on a spherical body in a rotational flow. *J Fluid Mech*. 1987;183:199-218.
82. Tomiyama A, Tamai H, Zun I, Hosokawa S. Transverse migration of single bubbles in simple shear flows. *Chem Eng Sci*. 2002;57:1849-1858.
83. Kashiwa B. On the Euler equations for multiphase flow. LA-UR-98831. Institute for Multiphase Science and Technology 1998 Annual Meeting, University of Santa Barbara, Santa Barbara, CA, Feb. 26-28; 1998.
84. Jackson R. *The Dynamics of Fluidized Particles*. New York, NY: Cambridge Univ. Press; 2000.
85. Johri J, Glasser BJ. Connections between density waves in fluidized beds and compressible flows. *AIChE J*. 2002;48:1645-1664.
86. Chen W, Hasegawa T, Tsutsumi A, Otawara K. Scale-up effects on the time-averaged and dynamic behavior in bubble column reactors. *Chem Eng Sci*. 2001;56:6149-6155.
87. Ruzicka MC, Drahoš J, Fialová M, Thomas NH. Effect of bubble column dimensions on flow regime transition. *Chem Eng Sci*. 2001;56:6117-6124.
88. Forret A, Schweitzer J-M, Gauthier T, Krishna R, Schweich D. Influence of scale on the hydrodynamics of bubble column reactors: An experimental study in columns of 0.1, 0.4, and 1 m diameters. *Chem Eng Sci*. 2003;58:719-724.
89. Sanyal J, Marchisio DL, Fox RO, Dhanasekharan K. On the comparison between population balance models for CFD simulation of bubble columns. *Ind Eng Chem Res*. 2004;DOI is: 10.1021/ie 049555.

Appendix A: Lift, Rotation, and Strain Forces in CFDLib

As discussed previously, the sum of the interfacial forces for the dispersed phase is expressed by

$$\sum_f \boldsymbol{F}_f = \boldsymbol{F}_D + \boldsymbol{F}_{rot} + \boldsymbol{F}_L + \boldsymbol{F}_{vm} + \boldsymbol{F}_S \tag{A1}$$

in which the lift, rotation, and strain forces are, respectively,

$$\boldsymbol{F}_L = \alpha_d \alpha_c \rho_v C_L (\boldsymbol{u}_d - \boldsymbol{u}_c) \times \nabla \times \boldsymbol{u}_c \qquad \text{(A2)}$$

$$\boldsymbol{F}_{rot} = \alpha_d \alpha_c \rho_v C_{rot} (\boldsymbol{u}_d - \boldsymbol{u}_c) \times \nabla \times \boldsymbol{u}_d \qquad \text{(A3)}$$

$$\boldsymbol{F}_S = \alpha_d \alpha_c \rho_v C_S [(\nabla \boldsymbol{u}_c + \nabla \boldsymbol{u}_d) + (\nabla \boldsymbol{u}_c + \nabla \boldsymbol{u}_d)^T] \cdot (\boldsymbol{u}_c - \boldsymbol{u}_d) \qquad \text{(A4)}$$

It should be noted that CFDLib does not require input values for the lift, rotation, and strain coefficients, C_L, C_{rot}, and C_S, respectively. Rather, input to the code requires values for the so-called attraction and repulsion coefficients, C_{att} and C_{rep}. These coefficients are used in calculating the attraction and repulsion forces accounted for in CFDLib[83]:

$$\boldsymbol{F}_{att} + \boldsymbol{F}_{rep} = \alpha_d \alpha_c \rho_v \boldsymbol{G} \cdot (\boldsymbol{u}_c - \boldsymbol{u}_d) \qquad \text{(A5)}$$

in which the matrix $\boldsymbol{G}$ is equal to

$$\boldsymbol{G} = C_{rep} \frac{1}{2} [(\nabla \boldsymbol{u}_c + \nabla \boldsymbol{u}_d) + (\nabla \boldsymbol{u}_c + \nabla \boldsymbol{u}_d)^T] - C_{att} [(\nabla \boldsymbol{u}_c + \nabla \boldsymbol{u}_d) - (\nabla \boldsymbol{u}_c + \nabla \boldsymbol{u}_d)^T] \qquad \text{(A6)}$$

The matrix $\boldsymbol{G}$ defined in Eq. A6 represents the sum of a symmetric strain-rate (or deformation) tensor and an antisymmetric tensor. By simple vector manipulations, the antisymmetric part can be expressed in an alternate form:

$$\begin{aligned} \boldsymbol{F}_{att} &= \alpha_d \alpha_c \rho_v (-C_{att}) [\nabla (\boldsymbol{u}_c + \boldsymbol{u}_d) - \nabla (\boldsymbol{u}_c + \boldsymbol{u}_d)^T] \cdot (\boldsymbol{u}_c - \boldsymbol{u}_d) \\ &= \alpha_d \alpha_c \rho_v (-C_{att}) (\boldsymbol{u}_c - \boldsymbol{u}_d) \times \nabla \times (\boldsymbol{u}_c + \boldsymbol{u}_d) \\ &= \alpha_d \alpha_c \rho_v (C_{att}) (\boldsymbol{u}_d - \boldsymbol{u}_c) \times \nabla \times (\boldsymbol{u}_c + \boldsymbol{u}_d) \qquad \text{(A7)} \end{aligned}$$

The final equality in Eq. A7 represents the sum of the lift force (Eq. A2) and the rotation force (Eq. A3), with $C_L = C_{rot} = C_{att}$. The symmetric part of $\boldsymbol{G}$ in Eq. A6 represents the sum of the strain-rate tensors for each phase:

$$\boldsymbol{S}_c + \boldsymbol{S}_d = \frac{1}{2} [\nabla (\boldsymbol{u}_c + \boldsymbol{u}_d) + \nabla (\boldsymbol{u}_c + \boldsymbol{u}_d)^T] \qquad \text{(A8)}$$

The resulting strain force is defined by the dot product between the strain-rate tensor and the relative velocity vector, as shown in Eq. A4, with $C_S = C_{rep}/2$.

It should be noted that the above discussion corresponds to CFDLib version 03.1. Our calculations were performed using CFDLib version 99.2, which defines the matrix $\boldsymbol{G}$ as

$$\boldsymbol{G} = C^*_{rep} [(\nabla \boldsymbol{u}_c + \nabla \boldsymbol{u}_d)^T] - C^*_{att} [(\nabla \boldsymbol{u}_c + \nabla \boldsymbol{u}_d) - (\nabla \boldsymbol{u}_c + \nabla \boldsymbol{u}_d)^T] \qquad \text{(A9)}$$

Corrections were made such that $\boldsymbol{G}$ would have the expected symmetric and antisymmetric tensors. However, choosing appropriate values for C^*_{rep} and C^*_{att} can allow the user to obtain the expected symmetric and antisymmetric parts of $\boldsymbol{G}$ by algebraic manipulation. This involves rewriting Eqs. A6 and A9 in the following manner:

$$\boldsymbol{G} = \left(\frac{C_{rep}}{2} - C_{att} \right) (\nabla \boldsymbol{u}_c + \nabla \boldsymbol{u}_d) + \left(\frac{C_{rep}}{2} + C_{att} \right) (\nabla \boldsymbol{u}_c + \nabla \boldsymbol{u}_d)^T \qquad \text{(A6}'\text{)}$$

$$\boldsymbol{G} = (-C^*_{att}) (\nabla \boldsymbol{u}_c + \nabla \boldsymbol{u}_d) + (C^*_{rep} + C^*_{att}) (\nabla \boldsymbol{u}_c + \nabla \boldsymbol{u}_d)^T \qquad \text{(A9}'\text{)}$$

If Eqs. A6′ and A9′ are assumed to be equivalent, then the coefficients can be related by

$$C_{att} = C^*_{att} + \frac{1}{2} C^*_{rep} \qquad C_{rep} = C^*_{rep} \qquad \text{(A10)}$$

Appendix B

Recall the continuity and momentum balance equations, respectively:

$$\frac{\partial \alpha_k \rho_k}{\partial t} + \nabla \cdot (\alpha_k \rho_k \boldsymbol{u}_k) = 0 \qquad \text{(B1)}$$

$$\begin{aligned} \alpha_k \rho_k \frac{\partial \boldsymbol{u}_k}{\partial t} + \alpha_k \rho_k \boldsymbol{u}_k \cdot \nabla \boldsymbol{u}_k &= -\alpha_k \nabla p + \nabla P_k + \alpha_k \rho_k \boldsymbol{g} \\ &+ \nabla \cdot \alpha_k \mu_{eff,k} [\nabla \boldsymbol{u}_k + (\nabla \boldsymbol{u}_k)^T] - \alpha_k \alpha_l \rho_c C_D(\mathrm{Re}) \frac{3}{4 d_b} |\boldsymbol{u}_k - \boldsymbol{u}_l| \\ &\times (\boldsymbol{u}_k - \boldsymbol{u}_l) - \alpha_k \alpha_l \rho_v C_{vm} \left[\left(\frac{\partial \boldsymbol{u}_k}{\partial t} + \boldsymbol{u}_k \cdot \nabla \boldsymbol{u}_k \right) - \left(\frac{\partial \boldsymbol{u}_l}{\partial t} \right.\right. \\ &\left.\left. + \boldsymbol{u}_l \cdot \nabla \boldsymbol{u}_l \right) \right] + \alpha_k \alpha_l \rho_v C_L (\boldsymbol{u}_k - \boldsymbol{u}_l) \times \nabla \times \boldsymbol{u}_c + \alpha_k \alpha_l \rho_v C_{rot} (\boldsymbol{u}_k \\ &- \boldsymbol{u}_l) \times \nabla \times \boldsymbol{u}_d + \alpha_k \alpha_l \rho_v C_S [(\nabla \boldsymbol{u}_k + \nabla \boldsymbol{u}_l) + (\nabla \boldsymbol{u}_k \\ &+ \nabla \boldsymbol{u}_l)^T] \cdot (\boldsymbol{u}_l - \boldsymbol{u}_k) \qquad \text{(B2)} \end{aligned}$$

The two-fluid model can be made dimensionless by using the volume-averaged slip velocity $\bar{U}_S$ for the characteristic velocity, the bubble diameter d_b for the characteristic length, and the continuous phase molecular viscosity $\mu_{0,c}$ for the characteristic viscosity. Additionally, the characteristic density used is ρ_c and the characteristic time is set to $(d_b/\bar{U}_S)$. Thus,

$$x^* = \frac{x}{d_b} \rightarrow x = x^* d_b \qquad \boldsymbol{u}^*_k = \frac{\boldsymbol{u}_k}{\bar{U}_S} \rightarrow \boldsymbol{u}_k = \boldsymbol{u}^*_k \bar{U}_S$$

$$\rho^*_k = \frac{\rho_k}{\rho_c} \rightarrow \rho_k = \rho^*_k \rho_c$$

$$t^* = \frac{t}{(d_b/\bar{U}_S)} \rightarrow t = \frac{t^* d_b}{\bar{U}_S}$$

$$\mu^*_{eff,k} = \frac{\mu_{eff,k}}{\mu_{0,c}} \rightarrow \mu_{eff,k} = \mu^*_{eff,k}\mu_{0,c}$$

$$p^* = \frac{p}{\rho_c(\bar{U}_S)^2} \rightarrow p = p^*\rho_c(\bar{U}_S)^2$$

$$P^*_k = \frac{P_k}{\rho_c(\bar{U}_S)^2} \rightarrow P_k = P^*_k\rho_c(\bar{U}_S)^2$$

$$\boldsymbol{g}^* = \boldsymbol{g}\frac{1}{d_b}\left(\frac{d_b}{\bar{U}_S}\right)^2 = \frac{\boldsymbol{g}d_b}{(\bar{U}_S)^2} \rightarrow \boldsymbol{g} = \boldsymbol{g}^*\frac{(\bar{U}_S)^2}{d_b}$$

Thus, the continuity and momentum balance equations in dimensionless form are, respectively,

$$\frac{\partial\alpha_k\rho^*_k}{\partial t^*} + \nabla\cdot(\alpha_k\rho^*_k\boldsymbol{u}^*_k) = 0 \tag{B3}$$

$$\begin{aligned}\alpha_k\rho^*_k\frac{\partial\boldsymbol{u}^*_k}{\partial t^*} + \alpha_k\rho^*_k\boldsymbol{u}^*_k\cdot\boldsymbol{\nabla}\boldsymbol{u}^*_k = -\alpha_k\boldsymbol{\nabla}p^* + \boldsymbol{\nabla}P^*_k + \alpha_k\rho^*_k\boldsymbol{g}^*\\ + \frac{1}{\mathrm{Re}}\boldsymbol{\nabla}\cdot\alpha_k\mu^*_{eff,k}[\boldsymbol{\nabla}\boldsymbol{u}^*_k + (\boldsymbol{\nabla}\boldsymbol{u}^*_k)^T] - \alpha_k\alpha_l\rho^*_cC_D(\mathrm{Re})\frac{3}{4d^*_b}|\boldsymbol{u}^*_k\\ - \boldsymbol{u}^*_l|(\boldsymbol{u}^*_k - \boldsymbol{u}^*_l) - \alpha_k\alpha_l\rho^*_vC_{vm}\left[\left(\frac{\partial\boldsymbol{u}^*_k}{\partial t^*} + \boldsymbol{u}^*_k\cdot\boldsymbol{\nabla}\boldsymbol{u}^*_k\right)\right.\\ \left. - \left(\frac{\partial\boldsymbol{u}^*_l}{\partial t^*} + \boldsymbol{u}^*_l\cdot\boldsymbol{\nabla}\boldsymbol{u}^*_l\right)\right] + \alpha_k\alpha_l\rho^*_vC_L(\boldsymbol{u}^*_k - \boldsymbol{u}^*_l)\times\boldsymbol{\nabla}\times\boldsymbol{u}^*_c\\ + \alpha_k\alpha_l\rho^*_vC_{rot}(\boldsymbol{u}^*_k - \boldsymbol{u}^*_l)\times\boldsymbol{\nabla}\times\boldsymbol{u}^*_d + \alpha_k\alpha_l\rho^*_vC_S\\ \times[(\boldsymbol{\nabla}\boldsymbol{u}^*_k + \boldsymbol{\nabla}\boldsymbol{u}^*_l) + (\boldsymbol{\nabla}\boldsymbol{u}^*_k + \boldsymbol{\nabla}\boldsymbol{u}^*_l)^T]\cdot(\boldsymbol{u}^*_l - \boldsymbol{u}^*_k)\end{aligned} \tag{B4}$$

Note that the dimensionless numbers appearing in the two-fluid model are Re and the force-model coefficients (which may depend on Re).

Manuscript received Mar. 4, 2004, and revision received Oct. 24, 2004.